https://ntrs.nasa.gov/search.jsp?R=20140010228 2019-08-31T20:03:14+00:00Z

The Astrophysical Journal, 753:52 (17pp), 2012 July 1 doi:10.1088/0004-637X/753/1/52
© 2012. The American Astronomical Society. All rights reserved. Printed in the U.S.A.

QUASI-PERIODIC FAST-MODE WAVE TRAINS WITHIN A GLOBAL EUV WAVE AND SEQUENTIAL TRANSVERSE OSCILLATIONS DETECTED BY *SDO*/AIA

Wei Liu[1,2], Leon Ofman[3,4,5], Nariaki V. Nitta[1], Markus J. Aschwanden[1], Carolus J. Schrijver[1], Alan M. Title[1], and Theodore D. Tarbell[1]
[1] Lockheed Martin Solar and Astrophysics Laboratory, 3251 Hanover Street, Palo Alto, CA 94304, USA; weiliu@lmsal.com
[2] W. W. Hansen Experimental Physics Laboratory, Stanford University, Stanford, CA 94305, USA
[3] Department of Physics, Catholic University of America, Washingtom, DC 20064, USA
[4] NASA Goddard Space Flight Center, Code 671, Greenbelt, MD 20771, USA
Received 2012 March 9; accepted 2012 April 24; published 2012 June 13

ABSTRACT

We present the first unambiguous detection of quasi-periodic wave trains within the broad pulse of a global EUV wave (so-called EIT wave) occurring on the limb. These wave trains, running *ahead of* the lateral coronal mass ejection (CME) front of 2–4 times slower, coherently travel to distances $\gtrsim R_\odot/2$ along the solar surface, with initial velocities up to 1400 km s^{-1} decelerating to ~650 km s^{-1}. The rapid expansion of the CME initiated at an elevated height of 110 Mm produces a strong downward and lateral compression, which may play an important role in driving the primary EUV wave and shaping its front forwardly inclined toward the solar surface. The wave trains have a dominant 2 minute periodicity that matches the X-ray flare pulsations, suggesting a causal connection. The arrival of the leading EUV wave front at increasing distances produces an uninterrupted chain sequence of deflections and/or transverse (likely fast kink mode) oscillations of local structures, including a flux-rope coronal cavity and its embedded filament with delayed onsets consistent with the wave travel time at an elevated (by ~50%) velocity within it. This suggests that the EUV wave penetrates through a topological separatrix surface into the cavity, unexpected from CME-caused magnetic reconfiguration. These observations, when taken together, provide compelling evidence of the fast-mode MHD wave nature of the *primary (outer) fast component* of a global EUV wave, running ahead of the *secondary (inner) slow* component of CME-caused restructuring.

Key words: Sun: activity – Sun: corona – Sun: coronal mass ejections (CMEs) – Sun: flares – Sun: oscillations – waves

Online-only material: animations, color figures

1. INTRODUCTION

Waves or traveling disturbances on *global* scales in the magnetized solar atmosphere have been a subject of intensive study over the past half century, partly because of their possible roles in transporting energy and diagnostic potential in inferring physical conditions on the Sun via coronal seismology (Uchida 1970; Roberts et al. 1984; Aschwanden 2004; Nakariakov & Verwichte 2005).

1.1. Global EUV ("EIT") Waves

One of the most spectacular traveling disturbances in the corona is expanding extreme-ultraviolet (EUV) enhancements across a large fraction of the solar disk, discovered by the *Solar and Heliospheric Observatory* (*SOHO*) EUV Imaging Telescope (EIT) and often called "EIT waves" (Moses et al. 1997; Thompson et al. 1998) or *global EUV waves*, which we adopt in this paper (or "EUV waves" for short). Their counterparts were also imaged at other wavelengths, including soft X-rays (Khan & Aurass 2002; Narukage et al. 2002) and radio emission (Warmuth et al. 2004; White & Thompson 2005). Traveling disturbances in the chromosphere were detected in Hα (Moreton 1960; Uchida 1968; Balasubramaniam et al. 2010) and He I λ10803 lines (Vršnak et al. 2002; Gilbert & Holzer 2004).

Global coronal seismology using large-scale EUV waves (Ballai 2007), compared with local seismology using loop oscillations, has been little explored because of their poorly understood origin and nature. Proposed mechanisms include *fast-mode magnetohydrodynamic (MHD) waves* as the coronal counterpart of chromospheric Moreton waves (Thompson et al. 1999; Wills-Davey & Thompson 1999; Wang 2000; Wu et al. 2001; Warmuth et al. 2001; Ofman & Thompson 2002; Grechnev et al. 2011a, 2011b) and coronal mass ejection (CME) produced *current shells or successive restructuring of field lines* (Delannée 2000; Delannée et al. 2008; Chen et al. 2002, 2005, 2011; Attrill et al. 2007; Dai et al. 2010). Fast modes, for example, as the only MHD waves that can propagate perpendicular to magnetic fields, can readily explain the semi-circular shape of global EUV waves and their observed reflection from coronal holes and refraction around active regions (Thompson & Myers 2009; Gopalswamy et al. 2009; Schmidt & Ofman 2010; Li et al. 2012b; Olmedo et al. 2012; Kienreich et al. 2012). Details of relevant observations and models can be found in recent reviews (Warmuth 2007, 2011; Vršnak & Cliver 2008; Wills-Davey & Attrill 2009; Gallagher & Long 2011; Zhukov 2011; Chen 2011; Patsourakos & Vourlidas 2012).

Early observations of global EUV waves were limited by instrumental capacities, particularly the low cadence of EIT (12–18 minutes) and the small field of view (FOV) of the *Transition Region and Coronal Explorer* (*TRACE*). These constraints were alleviated by the *STEREO*/EUV Imagers (EUVI; Wuelser et al. 2004) from two vantage points at improved cadence of 150 s, occasionally 75 s (e.g., Veronig et al. 2008, 2010; Patsourakos & Vourlidas 2009; Ma et al. 2009; Temmer et al. 2011; Muhr et al. 2011; Long et al. 2011b; Zhao et al. 2011; Li et al. 2012a). The more recent *Solar Dynamics Observatory* (*SDO*; Pesnell et al. 2012) Atmospheric Imaging Assembly

[5] Visiting Associate Professor, Department of Geophysics and Planetary Sciences, Tel Aviv University, Tel Aviv 69978, Israel.

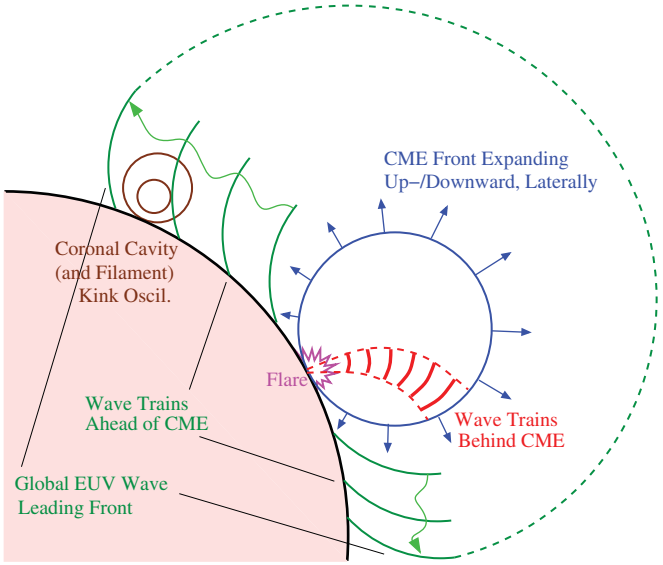

Figure 1. Schematic synopsis of the 2010 September 8–9 global EUV wave event, showing quasi-periodic wave trains running ahead of (green) and behind (red) the CME front (blue). The former is part of the broader EUV wave pulse that travels through a flux-rope coronal cavity, instigating its kink mode oscillations. The CME is initiated at an elevated height and produces a downward and lateral compression, driving the low-corona EUV wave. The wave trains behind the CME originate at the flare kernel, propagate along a narrow funnel, and terminate at the CME front.

(A color version of this figure is available in the online journal.)

(AIA; Lemen et al. 2012) observes the full corona at seven EUV wavelengths, covering a wide range of temperatures, at high cadence of 12 s and resolution of 1.″5. These capabilities have allowed us to study the kinematics and thermal structures of EUV waves in unprecedented detail (e.g., Liu et al. 2010; Chen & Wu 2011; Schrijver et al. 2011) and continue to shape a better understanding of this phenomenon, as we will see in the example presented here.

1.2. Introduction to This Study

Observations to date have generally shown a *single*, diffuse front in primary EUV waves (e.g., Wills-Davey et al. 2007). We report here the first unambiguous detection of *multiple*, quasi-periodic wave trains within a broad EUV wave pulse, as shown in the schematic of Figure 1. These wave trains, comprising fronts forwardly inclined toward the solar surface, are repeatedly launched ahead of the lateral CME front with a 2 minute periodicity and travel at velocities up to $\sim$1400 km s^{-1} (see Figure 5 and Section 3.2). We will show that the initial CME expansion produces a strong downward compression, previously unnoticed, which may play an important role in driving the EUV wave (see Section 3.1).

Filament oscillations (Okamoto et al. 2004; Hershaw et al. 2011; Tripathi et al. 2009) and loop deflections (Wills-Davey & Thompson 1999; Patsourakos & Vourlidas 2009; Liu et al. 2010; Aschwanden & Schrijver 2011) triggered by global EUV waves or Moreton waves have been observed at lower cadence or less favorable viewing angles (e.g., on the disk). AIA's *high cadence* allowed us to see, for the first time, an uninterrupted chain sequence of deflections and/or oscillations of various coronal structures *above the limb*, at increasing distances on the path of the global EUV wave. In particular, the wave travels across a topological separatrix surface into a coronal cavity

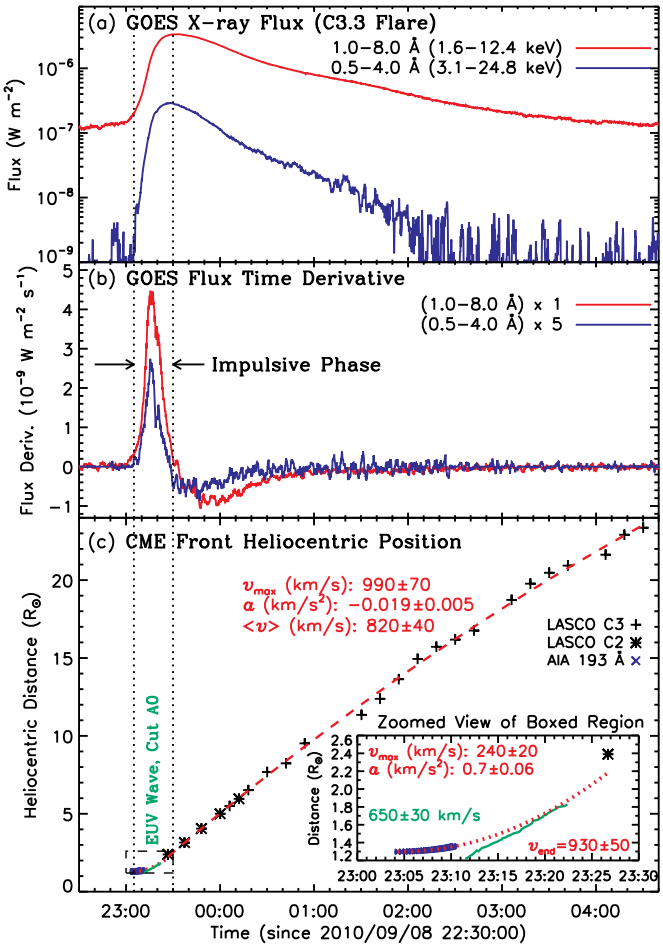

Figure 2. (a) *GOES* soft X-ray fluxes and (b) their time derivatives (smoothed with a 2 minute box car) for the C3.3 flare. (c) Heliocentric positions of the CME front detected by *SOHO*/LASCO C3 (plus signs) and C2 (asterisks) and AIA (blue crosses, reproduced from Figure 12(h)). The inset is an enlarged view of the boxed region during the flare impulsive phase when the CME acceleration and global EUV wave take place. Red broken lines are parabolic fits to the LASCO and AIA data labeled with fitted accelerations a and maximum velocities v_{max}. The green curve is the horizontal position of the northward global EUV wave front in the low corona, taken from Figure 10(a), which travels faster than the early CME.

(A color version of this figure is available in the online journal.)

hosting a filament at an elevated velocity and instigates its bodily oscillations (see Figure 6 and Section 4).

These new observations, when taken together, point to the true wave nature of the primary EUV wave. We organize this paper as follows. After an observational overview of the event under study in Section 2, we focus in Section 3 on the global EUV wave containing quasi-periodic wave trains running ahead of the CME, followed by Section 4 on successive structural oscillations on the wave path. In Section 5, we compare these wave trains with those in a coronal funnel behind the CME (Liu et al. 2011b) and flare pulsations. We conclude this paper with Section 6, followed by four Appendixes for our analysis techniques, the kinematics and temperature and height dependence of the EUV wave, and the early expansion of the CME and its role in wave generation.

2. OVERVIEW OF OBSERVATIONS

This event was observed by *SDO*/AIA on 2010 September 8–9 in the NOAA active region (AR) 11105 on the northwest

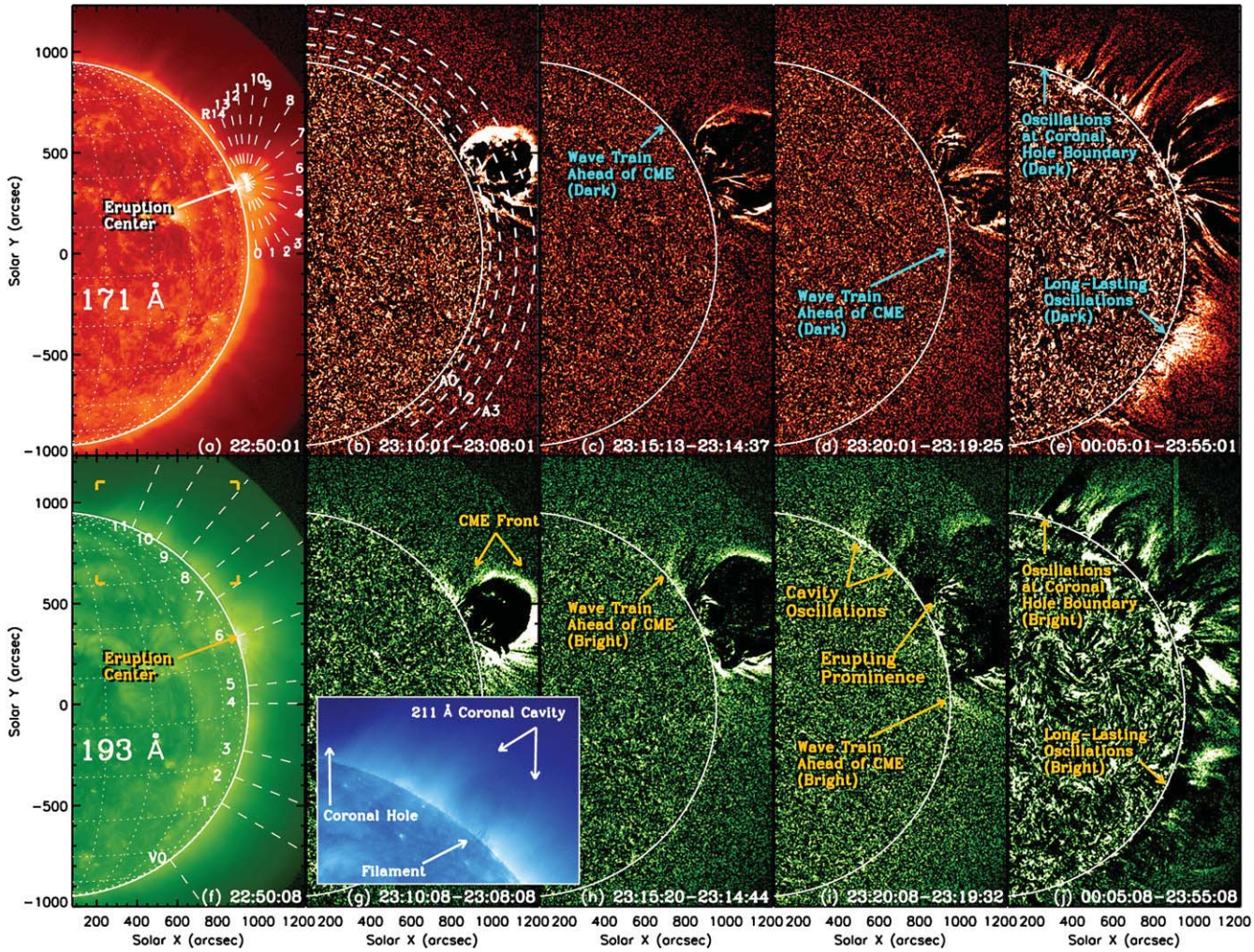

Figure 3. AIA images at 171 (red, top) and 193 Å (green, bottom), with original on the left (see movies 1A and 1B) and running difference on the right (see movie 1C for 193 Å). The dashed lines indicate radial cuts R0–R14 from the eruption center (a), azimuthal cuts A0–A3 (b), and vertical cuts V0–V11 (f) defined in Appendix A. Note EUV wave trains ahead of the CME front and oscillatory brightenings and darkenings anti-correlated at the two wavelengths. The four brackets in (f) marks the FOV of the enlarged inset at 211 Å (blue; see movie 1D) showing the coronal cavity and polar coronal hole.

(Animations and a color version of this figure are available in the online journal.)

limb. Around 22:40 UT (see movies 1A and 1B), the active region core starts gradual bulging, accompanied by the activation of a prominence that appears dark in EUV. At about 23:05 UT, the bulging evolves into a rapid expansion and leads to a CME expulsion. Simultaneously, the prominence erupts and unfolds itself, exhibiting unwinding twists (described for other events by, e.g., Liu et al. 2009b, 2009a, 2011a; Thompson et al. 2012).

A C3.3 class flare occurs at 23:00 UT, according to the *GOES* 1–8 Å soft X-ray flux, peaks at 23:33 UT, and then undergoes a slow decay for several hours (see Figure 2). *RHESSI* had a nighttime data gap during the flare. We thus use the spike of the *GOES* flux time derivative to define the *impulsive phase*, 23:05–23:30 UT. It is during this phase that a variety of phenomena, including the rapid CME acceleration (Zhang et al. 2001; Temmer et al. 2008) and the generation of the global EUV wave and quasi-periodic wave trains, take place.

By 23:10 UT, a dome-shaped CME front, identified as a bright rim surrounding a dimming region (e.g., Thompson et al. 2000a), has become evident in running difference images (see Figure 3). A few minutes later, a comparably weak intensity front appears in the *low* corona *ahead of* the CME flanks to the north and south. This weak, broad pulse, identified as a global EUV wave, contains quasi-periodic wave trains and propagates about 2–4 times faster than the lateral expansion of the CME. The northward EUV wave travels through a coronal cavity until it reaches the polar coronal hole boundary, instigating oscillatory brightenings. *Behind* the CME, additional quasi-periodic wave trains (Liu et al. 2011b) emanate from the flare along a funnel of coronal loops and fade away while approaching the CME front.

Major milestones of the event are listed in Table 1. We employed space–time diagrams, as detailed in Appendix A, to

Table 1
Event Timeline (2010 September 8–9)

22:40	AR core starts gradual bulging
23:05	Onset of rapid CME expansion
23:05–23:30	Flare impulsive phase
23:10–23:22	Flare X-ray pulsations (2 minute period)
23:11/23:14	Global EUV wave generated at 110 Mm to the north/south of the eruption center
23:11–23:23/ 23:14–23:26	Quasi-periodic wave trains launched ahead of CME at 110 Mm to the north/south of the eruption center
23:11–23:29	QFP wave trains launched from flare kernel behind CME
23:15–02:00+	Coronal cavity/filament oscillations

analyze various features, using four sets of narrow cuts (slits) shown in Figures 3 and 7. These cuts essentially form a user-defined coordinate system to sample images from complementing perspectives. The eruption center is defined at a height of 49″ (1″ = 0.731 Mm, $R_\odot$ = 952″) above the brightest flare kernel at N20°.6 on the limb.

3. GLOBAL EUV WAVE CONTAINING QUASI-PERIODIC WAVE TRAINS

Figure 4 gives an overview of the global EUV wave seen in space–time diagrams from azimuthal cuts A0 and A3. The general properties of the wave are examined in Appendix B. Here we summarize the key result.

1. *Temperature variations* (Appendix B1). In general, the EUV wave appears as a broad stripe of darkening at 171 Å and brightening at 193 and 211 Å, indicating prompt heating of plasma from 0.8 to 2.0 MK followed by restoring cooling, likely caused by adiabatic compression and subsequent rarefaction.
2. *Kinematics* (Appendix B2). Measured at 193 Å on the lowest cut A0 at height $h = 38''$, the leading front of the EUV wave travels with general deceleration at an average velocity of $650 \pm 30\,\mathrm{km\,s^{-1}}$ to the north and ~50% slower at $370 \pm 20\,\mathrm{km\,s^{-1}}$ to the south. We use such velocities to characterize the global EUV wave because the 193 Å wave generally signals the first arrival of the disturbance and no systematic height dependence of the wave velocity has been found.
3. *Height dependence* (Appendix B3). There is a clear trend of delayed arrival of the EUV wave at lower heights in the low corona ($h \lesssim 220$ Mm) near the eruption. This indicates a wave front forwardly inclined toward the coronal base.

3.1. EUV Wave Generation and Decoupling from CME

To probe the origin of the EUV wave, let us examine the enlarged space–time diagrams from all azimuthal cuts in Figure 5. The base ratio (top row) best shows the broad global EUV wave and post-CME dimming, while the running ratio (middle row) highlights fast varying features, such as the expanding CME/loops and quasi-periodic wave trains (see Section 3.2).

On the lowest cut A0, the global EUV wave is first detected some $s_0 = 150'' = 110$ Mm away to the north and south of the eruption center, but at different times. The northward wave appears at 23:11:20 UT, 6 minutes after the common onset of the fast CME expansion and flare impulsive phase, as described in Appendix C. By that time, the CME front to the north near the vertical direction has reached $>210\,\mathrm{km\,s^{-1}}$. The southward wave is generated 3 minutes later at the outermost edge of some low-lying loops rapidly pushing downward (Figures 12(m) and (n)). Within the distance s_0, no systematic emission change can be related to either the EUV wave or the CME expansion.

On higher cuts A1–A3 (Figure 5), while the EUV wave signal decreases, loop expansion due to the upwardly growing CME becomes increasingly evident. On cuts A2 and A3, the EUV wave can be traced further back in distance to near the eruption center and back in time as the successive onsets of the CME's rapid lateral expansion. This suggests that the EUV wave could be the continuation into the quiet-Sun region of the same disturbance signaling the fast expansion (cf. differential expansions in other events; Schrijver et al. 2008, 2011).

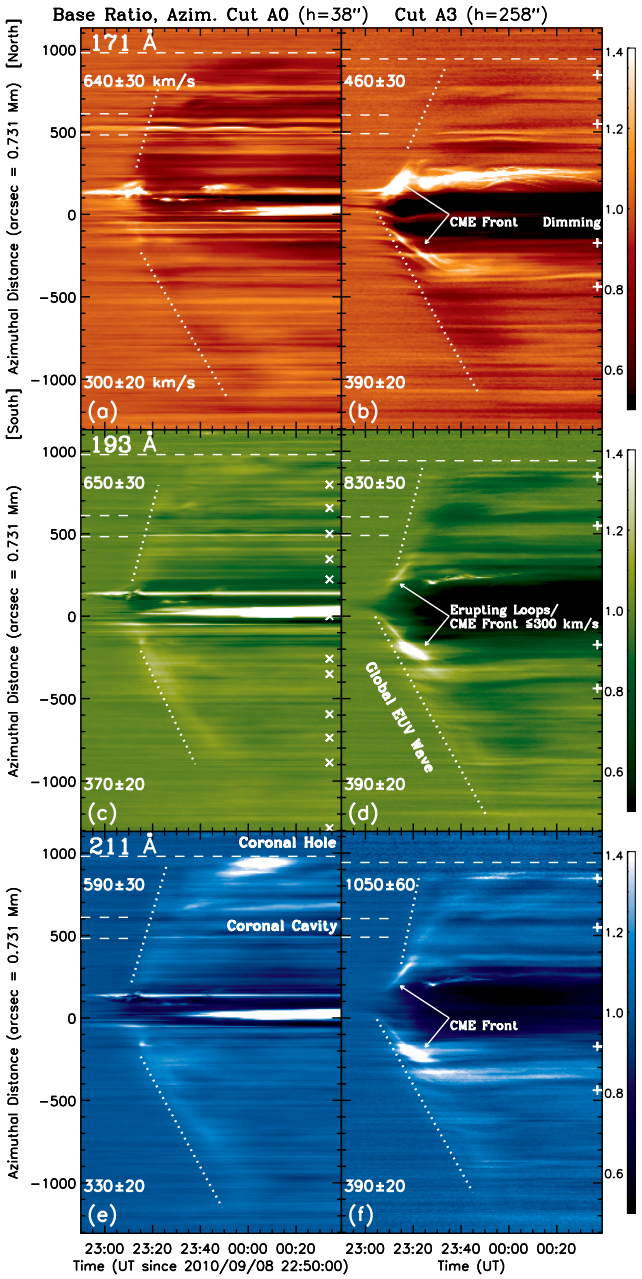

Figure 4. Base ratio space–time diagrams at 171 (red), 193 (green), and 211 Å (blue) from selected azimuthal cuts A0 and A3 defined in Figure 3(b). The distance is measured along each cut in the counterclockwise direction from the eruption center shown in Figure 3(a). Distances shown here are normalized to that on the lowest cut A0 to represent the azimuthal (latitudinal) position, a convention taken throughout this paper, while velocity measurements were based on the original distances. The dotted lines are linear fits to the global EUV wave front, labeled with fitted velocities (in $\mathrm{km\,s^{-1}}$). The horizontal dashed lines delineate the boundaries within each cut of the coronal cavity and polar coronal hole, best seen as dark areas in the 211 Å inset of Figure 3. The cross and plus signs on the right indicate the azimuthal positions of the vertical cuts defined in Figure 3(f) and of the temporal intensity profiles shown in Figure 9, respectively.
(A color version of this figure is available in the online journal.)

This rapid CME expansion may play a key role in driving the EUV wave, as described in Appendix C. It involves a sizable volume of roughly the active region of $r_{AR} = 110$ Mm in radius and originates at its center of a height $h_0 = 110$ Mm above the photosphere. Below this height, the CME expansion has a significant downward component, while the lateral expansion is negligibly slow and spatially confined (see Figure 12 and

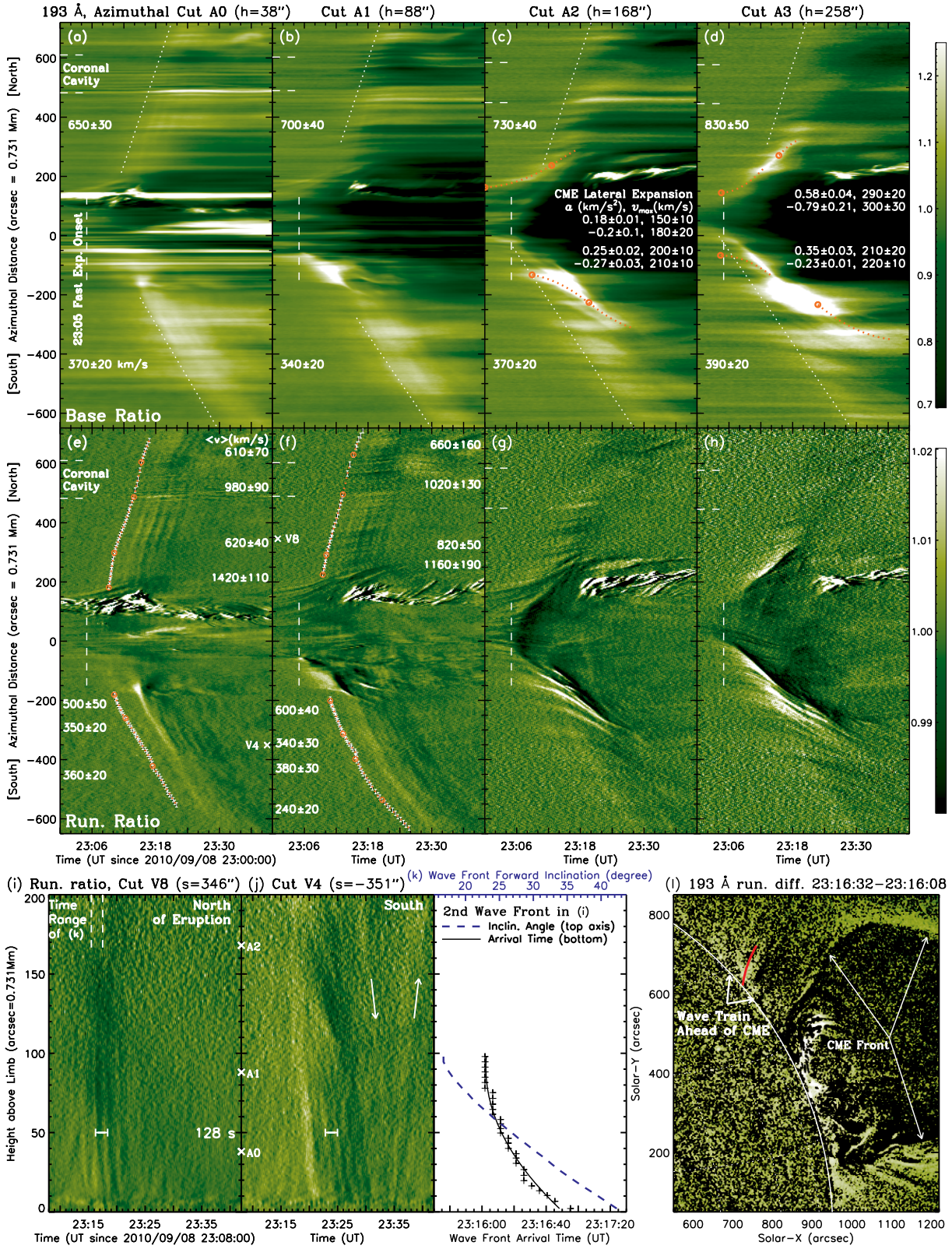

Figure 5. Enlarged 193 Å version of Figure 4 near the eruption from all azimuthal cuts in base ratio (top) and running ratio (middle). The red dotted lines in (c) and (d) are parabolic fits to the lateral CME front, with fitted accelerations (in $\mathrm{km\,s^{-2}}$) and maximum velocities (in $\mathrm{km\,s^{-1}}$) listed in the order of the start time of the fit (marked by an open circle). Note the acceleration followed by deceleration, making the CME fall behind the global EUV wave (white dotted lines). The vertical dashed line marks the onset of the flare impulsive phase and the rapid CME expansion at 23:05 UT. Note in (e) and (f) the quasi-periodic wave trains in the low corona to the north and south of the eruption, in which the white data points, shifted to the left by 5 minutes, are the positions of the most pronounced wave pulses, fitted with piecewise linear functions (red dotted lines) labeled by resulting velocities (in $\mathrm{km\,s^{-1}}$). Bottom: (i) and (j) Enlarged running-ratio version of Figure 11 for vertical cuts V8 and V4, showing delayed arrival at lower heights of the wave trains. (k) Arrival time (bottom x-axis) at cut V8 of the second wave front in (i) vs. height (y-axis). The blue dashed line (top x-axis) is the forward inclination angle from the local vertical of the reconstructed wave front, which is shown in red in the running difference image of (l).

(A color version of this figure is available in the online journal.)

movie 1C). Above this height, as shown in Figures 5(c) and (d), the lateral CME expansion experiences an acceleration phase with $a = (0.18 \pm 0.01)$–$(0.58 \pm 0.04)\,\mathrm{km\,s^{-2}}$ and maximum velocities (150 ± 10)–$(300 \pm 30)\,\mathrm{km\,s^{-1}}$, followed by a comparable deceleration. This makes the CME flanks quickly fall behind the global EUV wave that is 2–4 times faster, consistent with recently reported CME–wave decouplings (Patsourakos & Vourlidas 2009; Kienreich et al. 2009; Cheng et al. 2012).

The 110 Mm distance of the initial EUV wave from the eruption center is comparable to those of other EUV waves (e.g., Veronig et al. 2008; Liu et al. 2010) and Moreton waves or type II bursts (Warmuth et al. 2004; Muhr et al. 2010), suggesting a spatially extended rather than a point-like source region. Whether the EUV wave represents an MHD wave or CME-caused restructuring, such a considerable distance, in general, is required for the velocity and volume of the expanding CME (as the disturbance driver) to grow, in order to build up sufficient compression to the ambient corona to produce detectable emission changes. In addition, the associated 6–9 minute delay (cf. 1–2 minutes; Vršnak et al. 1995) seems reasonable for a piston-driven, nonlinear wave to steepen into a shock (Mann 1995; Vršnak & Lulić 2000; Bain et al. 2012), because it is on the same order of the predicted shock formation time (Žic et al. 2008, see, e.g., their Figure 6(a)) by applying relevant control parameters from our measurements.

3.2. Quasi-periodic Wave Trains ahead of CME

The quasi-periodic wave trains ahead of the CME appear as successive arc-shaped pulses in the low corona in running difference images (see Figures 3(h) and (i), movie 1C). They are best seen in running-ratio space–time diagrams (Figure 5, middle) as fine-structure, narrow stripes of alternating brightening and darkening, within the broader pulse of the global EUV wave seen in base ratio (top). The northward wave train is particularly evident, including coherent pulses traveling some 500″ ($\gtrsim R_\odot/2$) away. The first pulse in each direction is located at the leading front of the global wave, appearing at $s_0 = 150''$ from the eruption center ahead of the CME flank, followed by subsequent pulses originating from about the same location. Each pulse has the same wavelength dependence as the overall global wave noted above (see Appendix B1), indicating plasma heating.

The sharpness of these narrow pulses allowed us to trace detailed kinematics better than the diffuse front of the global EUV wave. We selected the most pronounced pulse from cuts A0 and A1 in each direction, i.e., the second in the north and the first in the south. We then fitted their space–time positions with a piecewise linear function, as shown in red in Figures 5(e) and (f), shifted by −5 minutes to allow the original data visible. On cut A0, the velocities within the first 1–2 minutes are 1420 ± 110 and $500 \pm 50\,\mathrm{km\,s^{-1}}$ in the north and south, respectively, and then drop by ∼50% to the average velocities of the diffuse wave front shown in panel (a). For the northward pulse, there is an additional velocity change upon its arrival at the coronal cavity, in which it travels at $980 \pm 90\,\mathrm{km\,s^{-1}}$, about 50% faster than the $620 \pm 40\,\mathrm{km\,s^{-1}}$ velocity outside, followed by a drop back to this level upon its exit from the cavity's far side. Such non-monotonic velocity variations resemble those in other EUV waves under different circumstances (Zhukov et al. 2009; Li et al. 2012b). A similar behavior occurs on cut A1, but we found no systematic height dependence of the wave velocity.

The height distribution of the quasi-periodic wave trains can be seen in running-ratio space–time diagrams from vertical cuts V8 (northward) and V4 (southward), as shown in Figures 5(i) and (j). These waves are prominent in the low corona $h < 150'' \approx 110\,\mathrm{Mm}$, and their signals rapidly fall with height. At least five pulses (stripes), uniformly spaced in time by about 2 minutes (128 s), can be identified in each direction. These stripes have negative slopes, indicating delayed arrival at progressively lower heights and wave fronts forwardly inclined toward the solar surface, same as the overall global EUV wave noted above (see Appendix B3). To the south, the shallower slope is consistent with the lower propagation velocity and thus longer delays. The sudden change of slope from negative to positive at 23:35 UT is a possible indication of reflection of the wave at the coronal base.

The arrival time of the second pulse from cut V8, for example, is plotted against height (y-axis) in Figure 5(k) and fitted with a parabolic function (solid line), indicating a delay of 53 s over a height range of 98″. As detailed in Appendix B3, we backtracked in time this delayed arrival to reconstruct the wave front seen in the running difference movie 1C that is, however, difficult to identify in stills. The result is shown in red in panel (l). Its forward inclination angle from the local vertical is shown in blue in panel (k), which increases with decreasing height, ranging from 17° at $h = 98''$ to 42° at the coronal base.

4. SEQUENTIAL OSCILLATIONS ON WAVE PATH

As mentioned earlier, upon the arrival of the global EUV wave at increasing distances, local coronal structures are sequentially deflected, setting off transverse oscillations, which are best seen as sinusoidal stripes in enlarged base-ratio space–time diagrams (Figure 6). In running-ratio diagrams (Figures 5, middle), they appear as numerous shallow-sloped, narrow stripes superimposed on the steep, broad pulse of the global EUV wave, as noted in an earlier event (Liu et al. 2010, see their Figure 5(d)). We found oscillations lasting up to 6 hr in a variety of structures, including the northern polar coronal hole boundary, with velocity amplitudes of 8–27 $\mathrm{km\,s^{-1}}$ and periods ranging from 12 minutes in short loops to 80 minutes in large-scale loops. We expect to use such high-resolution measurements as seismological tools in the future to infer physical conditions and damping mechanisms (e.g., Ofman & Aschwanden 2002; Ofman 2009; White & Verwichte 2012; Wang et al. 2012). Here we focus on the best manifestation of such oscillations in the coronal cavity to shed light on the nature of the EUV wave.

4.1. Oscillations of the Coronal Cavity

We selected three dark filament threads (labeled Osc. 0, 1, and 2) embedded in the coronal cavity as tracers of its oscillations seen in Figure 6. We obtained the space–time position $s(t)$ at the center of each thread, using its width as the spatial uncertainty. $s(t)$ was smoothed to approximate the slowly drifting equilibrium position $s_{\mathrm{eq}}(t)$, which was then removed to obtain the net oscillatory displacement $\Delta s(t) = s(t) - s_{\mathrm{eq}}(t)$, as shown in Figure 6(d). We fitted $\Delta s(t)$ with a damped sine function, $\Delta s(t) = A \exp[-(t-t_0)/\tau_A] \sin[2\pi(t-t_0)/P]$, shown as the red solid line, where A is the initial amplitude at $t = t_0$, P is the period, and τ_A is the e-folding damping time. These filament threads, although located at different positions, have fitted parameters in a narrow range, indicating a coherence consistent with the bodily oscillations of the entire cavity. The average parameters are $\langle \tau_A \rangle = (119 \pm 14)$ minutes, $\langle P \rangle = (27.6 \pm 0.1)$ minutes, and $\langle A \rangle = 3\farcs2 \pm 0\farcs1 = (2.3 \pm 0.1)\,\mathrm{Mm}$, giving an initial velocity amplitude $\langle v \rangle = \langle 2\pi A/P \rangle = (8.8 \pm 0.4)\,\mathrm{km\,s^{-1}}$.

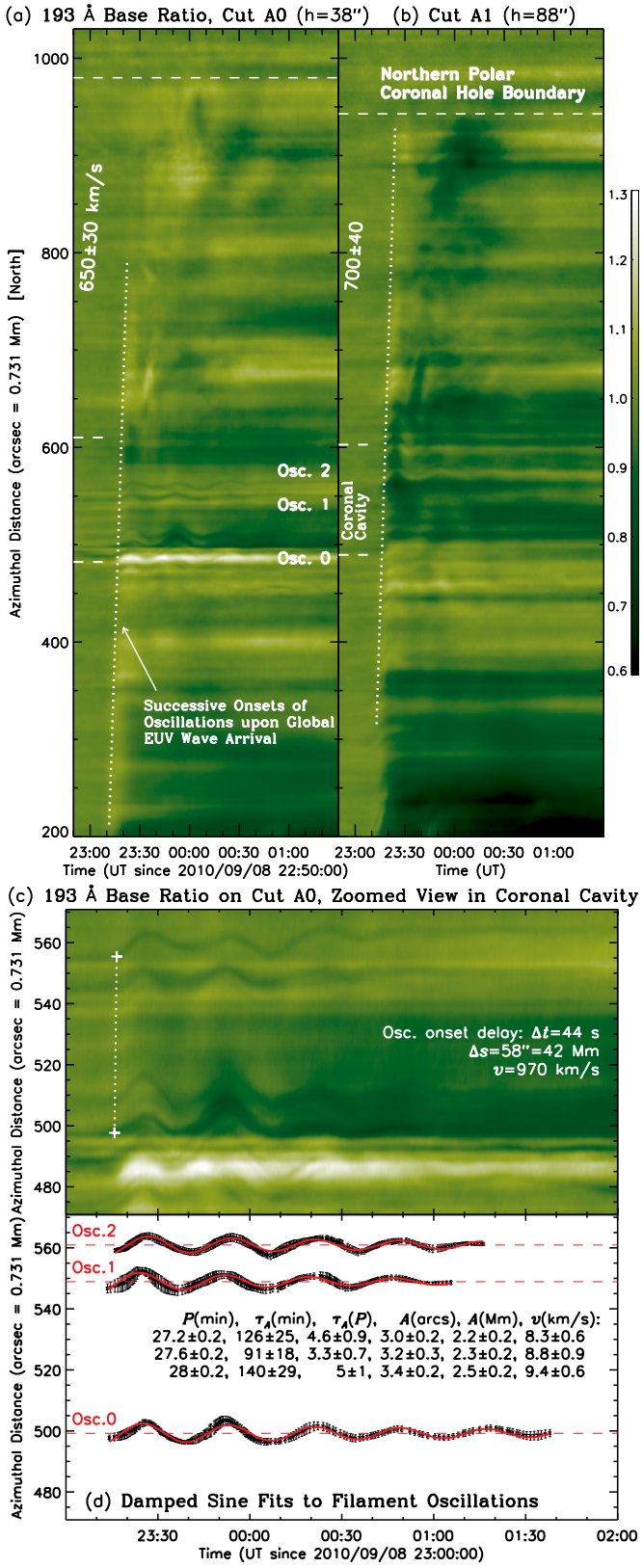

Figure 6. (a) and (b) 193 Å base ratio space–time diagrams along azimuthal cuts A0 and A1 to the north of the eruption, showing an uninterrupted sequence of transverse oscillations set off by the arrival of the global EUV wave at increasing distances. (c) Zoomed view of (a) showing filament oscillations within the coronal cavity, fitted with damped sine functions in (d). Note in (c) the delayed onsets of oscillations at greater distances in agreement with the EUV wave travel time at the measured velocity.

(A color version of this figure is available in the online journal.)

The onsets of oscillations within the cavity farther away from the eruption are delayed in time. For example, Osc. 2 at $\Delta s = 58'' = 42$ Mm from Osc. 0 is delayed by $\Delta t = 44$ s. This translates to a velocity of $\Delta s/\Delta t = 970\,\mathrm{km\,s^{-1}}$, in agreement with the elevated velocity of the wave trains within the cavity found earlier (see Figure 5(e)).

As detailed in Appendix D, we estimated the energies of the cavity oscillations and global EUV wave to be 10^{27} and 10^{28} erg, respectively, significantly lower than the 10^{31} erg kinetic energy of the CME. The transverse oscillations of the cavity are likely fast kink modes. Its magnetic field was thus estimated via coronal seismology to be on the order of ~6 G with a pitch angle of ~70°, suggestive of a highly twisted flux rope.

5. COMPARING TWO TYPES OF QUASI-PERIODIC WAVE TRAINS

We now examine the quasi-periodic wave trains within the funnel *behind* the CME and flare pulsations to help understand the wave trains in the global EUV wave *ahead of* the CME presented in Section 3.2.

5.1. QFP Wave Trains in Funnel behind CME

Figure 7 (top panels, see movies 2A and 2B) shows the quasi-periodic wave trains behind the CME as successive arc-shaped intensity variations on the 1%–5% level, traveling along a funnel of coronal loops rooted at the flare kernel and curved toward the south. No significant signals can be detected in channels other than 171 Å, suggesting that the responsible plasma is likely near this channel's peak response temperature of 0.8 MK. In space–time diagrams (bottom panels), these waves are steep, recurrent stripes behind the bright CME front. Parabolic fits (dotted lines) to a prominent wave pulse in different directions indicate large decelerations of 3–4 $\mathrm{km\,s^{-2}}$, with initial velocities at $s_0 = 150''$ from the flare kernel of (1020 ± 130)–$(1240 \pm 160)\,\mathrm{km\,s^{-1}}$, which are comparable to those of the northward quasi-periodic waves ahead of the CME, but twice those of the southward waves (see Figure 5(e)).

We identify the wave trains in the funnel as quasi-periodic fast propagating (QFP) waves recently discovered by AIA (Liu et al. 2010, 2011b; Shen & Liu 2012) and confirmed as fast-mode magnetosonic waves in three-dimensional MHD simulations (Ofman et al. 2011). The new characteristics found here are the rapid deceleration and disappearance while approaching the CME front, which will be discussed in Section 6.2.

5.2. Fourier Analysis of Wave Trains behind/ahead of CME and Flare Pulsations

We now apply Fourier analysis to the quasi-periodic waves both ahead of and behind the CME front and compare them with flare pulsations. From each of the space–time diagrams shown in Figure 8 (left), we extracted a data cube from the dashed box in which the wave signals are prominent. We then obtained its Fourier power (k–ω diagram) in the domain of temporal frequency ν and spatial wavenumber k, as shown in the middle. Each k–ω diagram displays a bright ridge that represents the dispersion relation of the wave averaged over the extracted duration. Within a selected region enclosed by the dashed lines around the ridge, the (ν, k) positions of bright pixels above a threshold (10% of the maximum), weighted by the power, were fitted with a linear function. These fits (passing through the origin), as marked by the two cross signs on the sides, indicate average phase velocities of

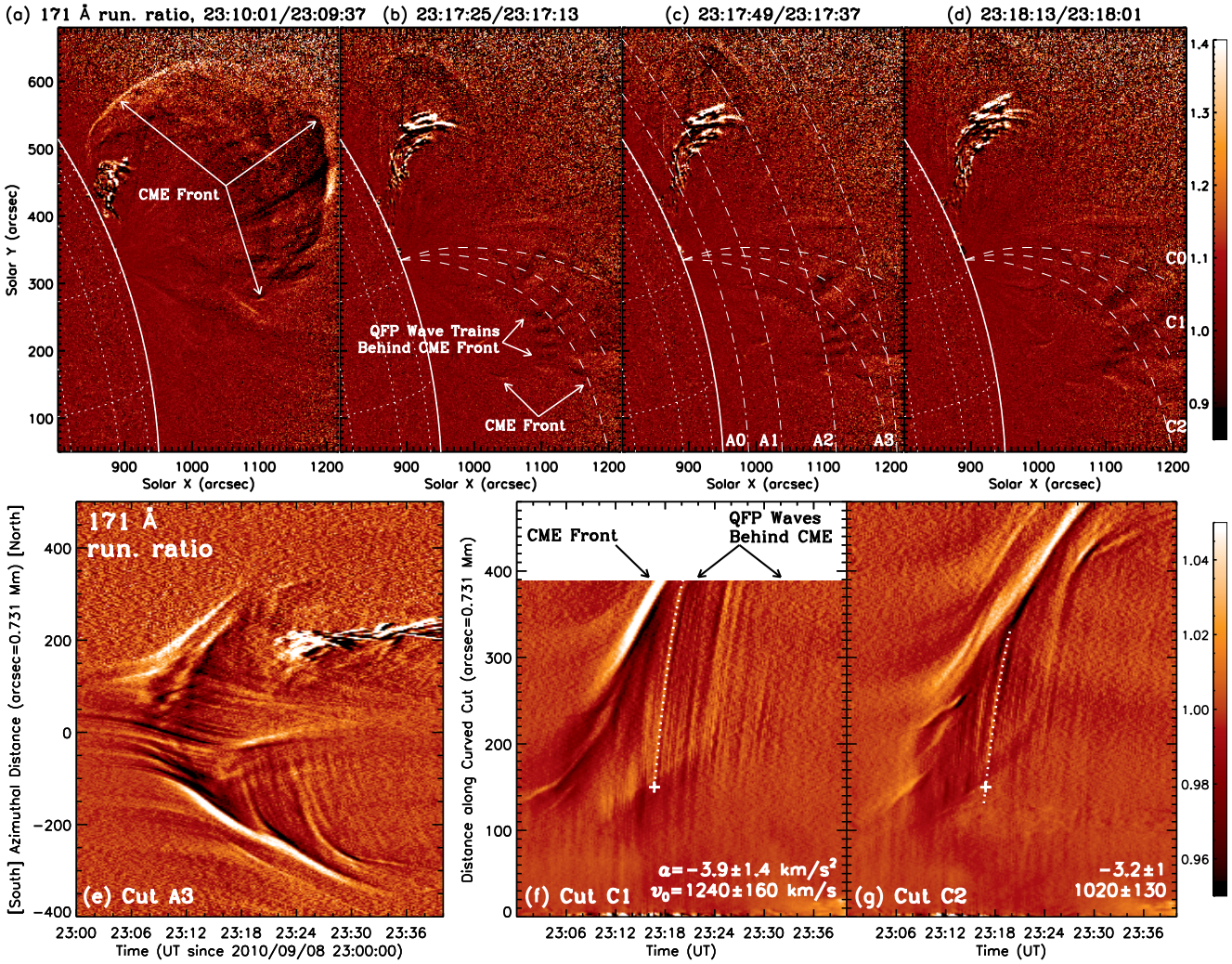

Figure 7. QFP wave trains seen at 171 Å in the funnel rooted at the flare kernel behind the CME front. Top: running-ratio images (see movies 2A for original and 2B for running difference). The dashed (dot-dashed) lines mark the curved cuts C0–C2 (azimuthal cuts A0–A3). Bottom: running-ratio space–time diagrams from selected azimuthal cut A3 and curved cuts C1 and C2. Overlaid dotted lines are parabolic fits to a single wave front seen in the respective cuts, labeled with fitted deceleration a and initial velocity v_0 at a reference distance of $s_0 = 150''$ (plus sign).

(Animations and a color version of this figure are available in the online journal.)

$v_{\rm ph} = 890 \pm 250,\ 670 \pm 140,\ -380 \pm 140\,{\rm km\,s^{-1}}$, which agree with the corresponding velocities measured in the space–time diagrams (see Figures 5 and 7). Here the +/− signs denote the propagation direction and the uncertainties imply scatter due to temporal variations.

By averaging Fourier power over wave number k within the selected regions, we obtained the frequency distributions of these waves (Figures 8, right). Prominent peaks were fitted with Gaussians to find the corresponding frequencies (periods) and their 1σ uncertainties. As a general trend, the QFP waves behind the CME front are preferentially distributed at high frequencies, with the highest peak (marked by an asterisk) located at $\nu = 21 \pm 1$ mHz ($P = 47 \pm 2$ s), while the waves ahead of the CME are concentrated at low frequencies, with the highest peaks at 128 ± 18 and 212 ± 24 s for the north- and southward waves, respectively. The second-highest peak of the southward waves is at 159 ± 27 s, similar to the highest peak of the northward waves. We thus refer to both with a 2 minute periodicity. Such periodicities can also be visually identified in the space–time domain on the left.

In an earlier event (Liu et al. 2011b), a 3 minute period was found in both the QFP waves in a funnel and X-ray and UV flare pulsations (Ofman & Sui 2006; Nakariakov & Melnikov 2009; Sych et al. 2009). We searched for such a common periodicity in this event. Because of no hard X-ray coverage and limb occultation of UV ribbons here, we used the time derivative of the *GOES* 0.5–4 Å soft X-ray flux as a proxy of hard X-rays, assuming the Neupert (1968) effect at work (Veronig et al. 2005; Liu et al. 2006; Ning & Cao 2010). As shown in Figure 8(d), there are clear pulsations superimposed on a slower variation shown in red, which was then removed to give a detrended light curve shown in blue. We extracted the detrended data within the interval defined by the dashed box, covering most of the impulsive phase, and obtained its Fourier power (panel (l)). The power is primarily distributed within 3–23 mHz, with concentration at low frequencies or long periods (2–3.5 minutes). This trend is similar to that of the EUV waves ahead of the CME (panels (j) and (k)) but differs from that of the QFP waves behind the CME with stronger power at high frequencies (panel (i)). In particular, the prominent flare period of 143 ± 16 s agrees, within uncertainties, with the 2 minute periodicity of the waves ahead of the CME. The wavelet power (panel (h)) of the flare light curve shows a peak of such pulsations, five of which, marked by the vertical dotted lines, can be identified in panel (d). On the other

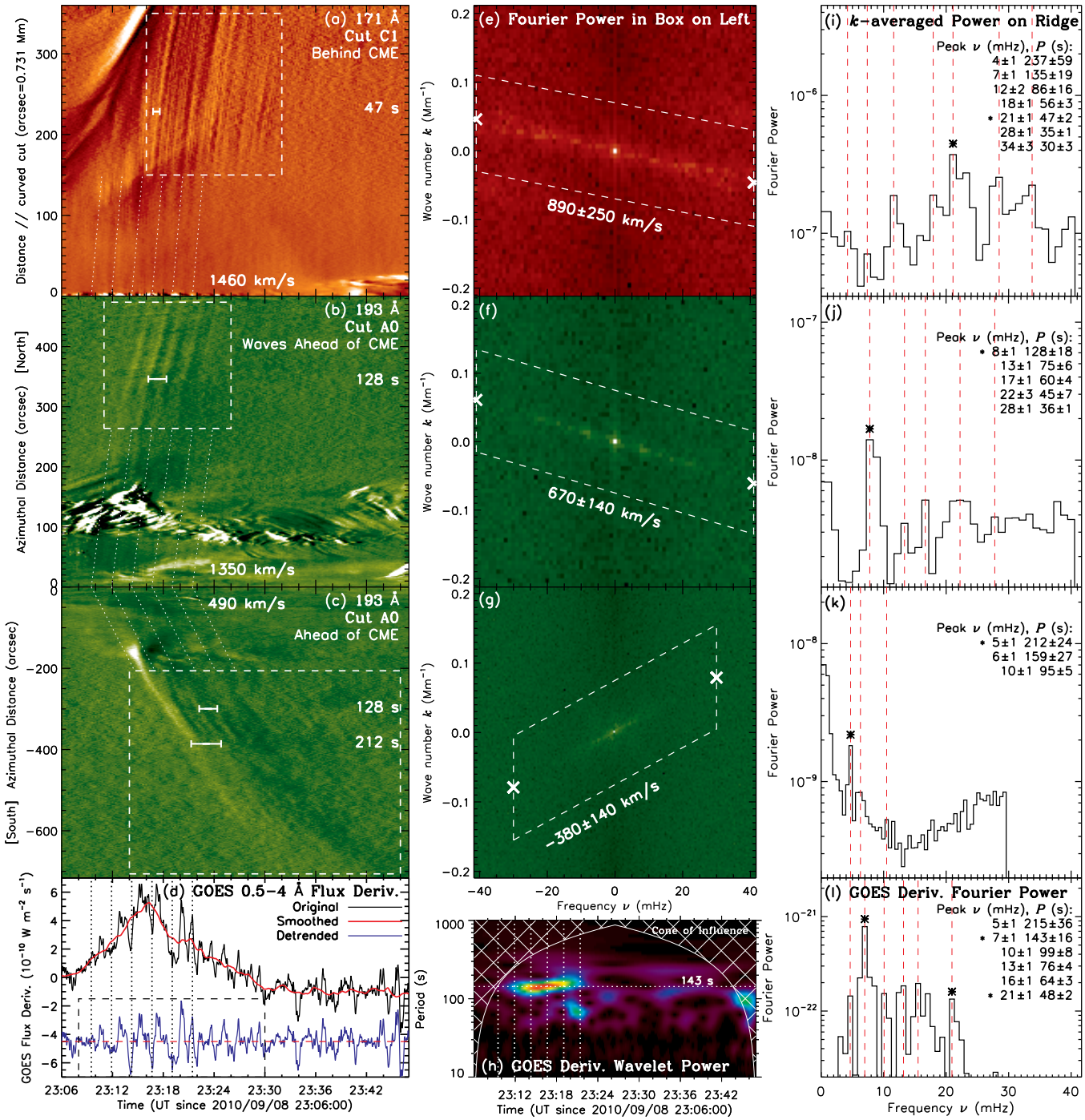

Figure 8. Fourier analysis of quasi-periodic waves and flare pulsations. Top three rows—left: running-ratio space–time diagrams from curved cut C1 at 171 Å (a) and azimuthal cut A0 at 193 Å to the north (b) and south (c) of the eruption, showing waves behind and ahead of the CME, respectively. Middle: Fourier power (k–ω diagram) on logarithmic scales of the data cube within the boxed region on the left. The cross signs mark the end points of a power-weighted linear fit to the bright ridge. Right: Fourier power averaged over wave number k within the parallelogram in the middle. The frequencies and periods of peaks identified by red vertical lines are listed on the right. Selected prominent peaks are marked by asterisks, and their periods are indicated by the horizontal bars on the left. Bottom row: (d) Time derivative of the *GOES* 0.5–4 Å flux. Subtracting the gradual, smoothed data (red solid line) gives the detrended blue curve, whose wavelet power and Fourier power (within the time range defined by the dashed box) are shown in (h) and (l), respectively. The vertical dotted lines mark five pulsations at the dominant 143 s period.

(A color version of this figure is available in the online journal.)

hand, despite their different general trends, the flare pulsations and the waves behind the CME share some common frequencies within their broad distributions, including a prominent peak at 21 ± 1 mHz or 47 ± 2 s.

We now return to the space–time domain to further explore the connections between the flare pulsations and the two groups of quasi-periodic EUV waves. In each space–time diagram of Figure 8 (left), we located the onset times of the first identified flare pulsation at the origin ($s = 0$, the flare kernel) and of the quasi-periodic waves at the distance of the near edge of the dashed box. We then connected the two positions with a straight dotted line, followed by parallel lines corresponding to the rest of the five pulsations at the 143 s period. Interestingly, these slanted lines translate to velocities of 1460, 1350, and

Table 2
General Properties of Phenomena Involved in the Event

Phenomena	v (km s^{-1})			Period	E (erg)
CME	Lateral 150–300		Vertical 990		10^{31}
Flare				2 minutes	
Wave Trains (WTs) ahead of CME (Global EUV Wave):					10^{28}
(1) Northward	Init. 1420	Ave. 650	In Cav. 980	2 minutes	
(2) Southward	500	370		2 minutes	
WTs behind CME	1020–1240			47 s	
Cavity Osc.	9			28 minutes	10^{27}

490 km s^{-1} that agree with the initial velocities of the respective wave trains noted earlier (see Figures 5 and 7). In addition, for the northward wave train ahead of the CME, the slanted lines closely trace the first two pulses and match the onsets of the rest of the five pulses at the edge of the box. For the southward waves, such a close match is less evident, but the duration of these flare pulsations extrapolated to the box edge overlaps with that of the quasi-periodic waves there. Implications of these coincidences will be discussed in Section 6.3.

6. CONCLUDING REMARKS

6.1. Summary

We have presented detailed analysis of a global EUV wave containing quasi-periodic wave trains ahead of the CME front, focusing on three interrelated aspects: the generation of the EUV wave and its decoupling from the CME, sequential structural oscillations (particularly of the coronal cavity) triggered by the wave, and a comparison of these wave trains with those behind the CME front and with flare pulsations. We summarize the general properties of various phenomena in Table 2 and recapitulate below our findings, the first two being reported for the first time.

1. *Quasi-periodic wave trains*[6] within the broad global EUV wave pulse travel ahead of the lateral CME front coherently to $\gtrsim R_\odot/2$ along the solar surface. Their initial velocity of 1420 ± 110 km s^{-1} (500 ± 50 km s^{-1}) to the north (south) of the eruption decelerates to their average velocity ~50% slower. Their dominant 2 minute period agrees with that of the X-ray flare pulsations. These wave trains are spatially confined to the low corona $h \lesssim 110$ Mm, similar to the heights of global EUV waves seen by *STEREO* (Patsourakos et al. 2009; Kienreich et al. 2009). Their arrival is delayed at lower heights by up to three minutes, indicating wave fronts being forwardly inclined toward the coronal base (see Figures 5 and 8, Section 3.2), while we found no systematic height dependence of the wave velocity (Figure 10).
2. *Sequential transverse oscillations* and deflections of local structures, upon the arrival of the global EUV wave at increasing distances, form an uninterrupted chain reaction. The best manifestation is the (likely fast kink mode) oscillations of the coronal cavity and its embedded filament, with a 28 minute period and 9 km s^{-1} velocity amplitude. The delayed oscillation onsets across the cavity agree with the travel time of the EUV wave at an elevated velocity of ~980 km s^{-1} within it. The estimated energies of the cavity oscillations and global EUV wave are 10^{27} and 10^{28} erg, respectively, 10^3–10^4 times lower than the 10^{31} erg kinetic energy of the CME (Figure 6, Section 4).
3. At low altitudes $h < 110$ Mm, the global EUV wave is first detected at $s_0 = 110$ Mm to the north and south of the eruption center, 6–9 minutes after the coincidental onset of the rapid CME expansion and flare impulsive phase. At higher altitudes, the EUV wave can be traced further back in distance to near the eruption center and back in time as the successive onsets of rapid loop expansions involved in the CME (Figure 5 and Section 3.1).
4. The fast expansion of the CME, with a significant downward component, involves a sizable volume of about the active region of 110 Mm in radius with its center at an elevated height of 110 Mm (Figure 12 and Appendix C). Negligibly slow near the coronal base, the lateral expansion grows with height, reaching 150–300 km s^{-1} and then decelerating, falling behind the global EUV wave of 2–4 times faster (Figure 5).
5. The broad global EUV wave and its narrow quasi-periodic pulses appear as darkening at 171 Å and brightening at 193 and 211 Å, with the maximum intensity variations being generally delayed from 193 to 211 and 171 Å, suggestive of heating from typically 0.8 to 2.0 MK followed by restoring cooling (Figures 4 and 9, Appendix B1).
6. There are additional QFP wave trains (fast magnetosonic; Liu et al. 2011b; Ofman et al. 2011) of a shorter, dominant period of 47 ± 2 s, traveling at 1000–1200 km s^{-1} along the coronal funnel rooted at the flare kernel *behind* the CME front, near which they abruptly disappear (Figure 7 and Section 5.1).

6.2. Proposed Physical Picture

We propose the following physical picture, as shown earlier in Figure 1, to tie together these observations. After a gradual rise and bulging of the active region of radius $r_{AR} = 150'' = 110$ Mm, a rapid expansion, likely driven by a Lorentz force, initiates near its center located at a height r_{AR} above the photosphere. Within minutes, this expansion soon involves the entire active region of a significant volume and becomes sufficiently fast ($\gtrsim$200 km s^{-1}), leading to a CME expulsion (Patsourakos et al. 2010b). An EUV wave is then generated in the low corona at the outer edge of the expanding CME, $s_0 = 110$ Mm from the eruption center. This distance and the 6–9 minute delay allow the CME expansion to grow and build up sufficient compression to the ambient corona or allow a nonlinear wave to steepen into a shock.

Initially centered at a significant height of 110 Mm, the expanding CME volume naturally produces the sphere-like shape of the early EUV wave front. The elevated lateral expansion and underlying chromosphere of extremely high density, essentially serving as a hard floor, compose an angled formation. Compared with the upward expansion into the open corona, this formation produces a compression to the surrounding low corona at an enhanced efficiency. This is similar to a piston in a semi-enclosed volume and may play an important role in driving the low-corona portion of the EUV wave that is forwardly inclined to the solar surface. The *downward* component of the compression[7] may cause on-disk

[6] Such wave trains were somewhat discernible in an earlier *STEREO* event at a lower cadence of 75 s but were not analyzed (Patsourakos et al. 2010a, see their Figure 11).

[7] As a possibility yet to be validated, such a downward compression could be physically similar to recently proposed Lorentz transients (Fisher et al. 2012) in flares that generate photospheric magnetic field changes (Wang & Liu 2010; Sun et al. 2012) and even sunquakes (Zharkov et al. 2011; Hudson et al. 2012).

redshifts in EUV waves (Harra et al. 2011; Veronig et al. 2011) and magnetic transients in Moreton waves (Kosovichev & Zharkova 1999). Such compression can explain the preferential height distribution of the EUV wave in the *low* corona and can produce density enhancements and adiabatic heating (Schrijver et al. 2011; Downs et al. 2012), which are likely responsible for the observed emission variations, perhaps together with other heating mechanisms. This adds to the importance of the lateral (versus vertical) CME expansion in EUV wave generation (Pomoell et al. 2008; Temmer et al. 2009).

As the CME expands and its center rises, the ambient corona parts to allow the CME expulsion into the heliosphere. Its lateral expansion at increasing heights then slows down and halts, partly because of the resistance of the ambience by a Lorentz restoring force. This produces a dimming region of a limited spatial extent. However, the EUV wave proceeds at the local fast-mode velocity to the rest of the corona, leading to the spatial decoupling from its initial driver, the CME. The periodicity (2 minutes) and coherence over great distances ($\gtrsim R_\odot/2$) of the wave trains within the broad global EUV wave pulse clearly indicate their true wave nature. Their velocities of 300–1400 km s^{-1} are also within the expected range of coronal fast-mode speeds. If the simulated "coronal Moreton waves" (Chen et al. 2002, 2005) repeatedly launched and running ahead of the CME flanks are real, our result provides the first observational evidence of such waves. As such, global EUV waves can no longer be considered as single-pulse disturbances as previous low-resolution observations indicated (Wills-Davey et al. 2007).

As the EUV wave propagates outward in all directions, the ambient coronal loops are sequentially displaced at increasing distances, with delays in agreement with wave travel times. These loops generally overshoot and start fast kink mode oscillations, again, driven by a Lorentz restoring force produced by the displaced magnetic field. These oscillations, signaling the *first* response to the arrival of the traveling disturbance, are another manifestation of its fast-mode wave nature that is the propagation of a perturbation at the *highest* velocity supported by the medium. The initial loop displacement takes place in the direction of the EUV wave propagation, further supporting its true wave nature (see, e.g., Figure 7 of Patsourakos & Vourlidas 2012). These oscillating loops do not participate in the CME expulsion but are only passively perturbed, while maintaining their topological integrity largely unchanged. They are thus not the footprint of a CME (cf. Attrill et al. 2007).

Upon arrival at the coronal cavity, the global wave front and subsequent quasi-periodic wave train continue to travel into it and exit from its far side. Their velocities within the cavity being 50% higher than outside indicate higher Alfvén and fast-mode speeds, expected from the lower plasma density and higher magnetic field strength in a flux-rope cavity (Gibson et al. 2010; Berger et al. 2011). In other words, the same disturbance travels into the cavity at velocities modified according to the local fast-mode speed. (If the wave were to bypass the cavity in front of or behind it in projection, one would not expect such a velocity change.) This also implies that this disturbance must have penetrated through a topological separatrix surface that separates the flux rope, as a distinct flux system, from the surrounding corona. This contradicts the prediction that a CME-caused apparent wave cannot travel across such a surface (Chen et al. 2002; Delannée et al. 2007). The EUV wave does, however, stop at the polar coronal hole boundary, another separatrix surface, as observed before (Thompson & Myers 2009). This is likely because of the strong reflection due to the large gradient of the wave speeds there (Schmidt & Ofman 2010). The lack of reflection signature at the coronal cavity may suggest a relatively small wave speed gradient and thus a large transmission (versus reflection) coefficient, which requires further investigation.

The QFP wave trains traveling along the coronal funnel likely originate from the flare, as previously found (Liu et al. 2011b), but with some different frequency distributions. They are spatially confined *within* the CME bubble, which may have produced a favorable condition for their generation and/or detection. Their sudden termination at the CME front is likely due to damping generated by the discontinuity there that rapidly dissipates these waves and/or due to increased dispersion associated with the decrease of the fast-mode speed with height, as predicted in three-dimensional MHD simulations (Ofman et al. 2011).

6.3. Discussion

The forward inclination of the early EUV wave front in the low corona has important implications (e.g., Grechnev et al. 2011b). An observational consequence is a delayed arrival by, e.g., tens of seconds to minutes, of its chromospheric counterpart, a Moreton wave, as indicated in recent preliminary results (White et al. 2011). While the early-stage EUV wave front is primarily shaped by its driver, as the wave travels farther away, the propagation effect will become increasingly influential. If the EUV wave is a true MHD wave, refraction can deflect its ray trajectory away from regions of high wave speeds toward regions of low wave speeds (Uchida 1968; Afanasyev & Uralov 2011). Therefore, the shape and temporal evolution of the EUV wave front have a seismological potential (Ballai 2007) to infer the spatial distribution of the fast-mode and Alfvén speeds and thus the coronal magnetic field strength.

The common periodicities of the quasi-periodic waves (especially those ahead of the CME) and flare pulsations and the consistent extrapolated velocities (see Section 5.2) point to the possibility that a cyclic disturbance, likely a fast-mode MHD wave, originates from the flare site (cf. Chen 2006) and modulates the EUV waves both *ahead of* and *behind* the CME. The different physical environments in which these waves propagate may further modify their relative amplitudes by, e.g., a combination of phase velocity variations and wave dispersion, giving rise to their different observed frequency distributions. We also note that no clear wave signatures can be identified within $\sim$150″ (100″) from the eruption center for the waves ahead of (behind) the CME front. We speculate this being caused by the line-of-sight integration of other more dominant features near the eruption and/or by disturbance amplitudes below the instrument sensitivity in the early stage. Another possibility for such common periodicities is fast kink mode oscillations of loops in the peripheral of the active region instigated by the CME eruption. In this case, the period $P = 2l/(Nc_k)$ for the fundamental mode ($N = 1$) gives the loop length $l = Pc_k/2 = (2\text{ minutes}) \times (1\text{ Mm s}^{-1})/2 \approx 60$ Mm, which is reasonable for large active region loops and comparable to the height range ($\sim$110 Mm, Figure 5(i)) of the low-corona wave trains. However, despite our best efforts, we could not identify such loop oscillations in AIA data. Alternatively, if these oscillations are not free, linear kink modes, but are driven or nonlinear, their periodicities would be determined by the driver or nonlinearity, not by the loop length. These aspects require further investigation with three-dimensional MHD models.

Recent observations (Harra & Sterling 2003; Zhukov & Auchère 2004; Kienreich et al. 2009; Patsourakos & Vourlidas

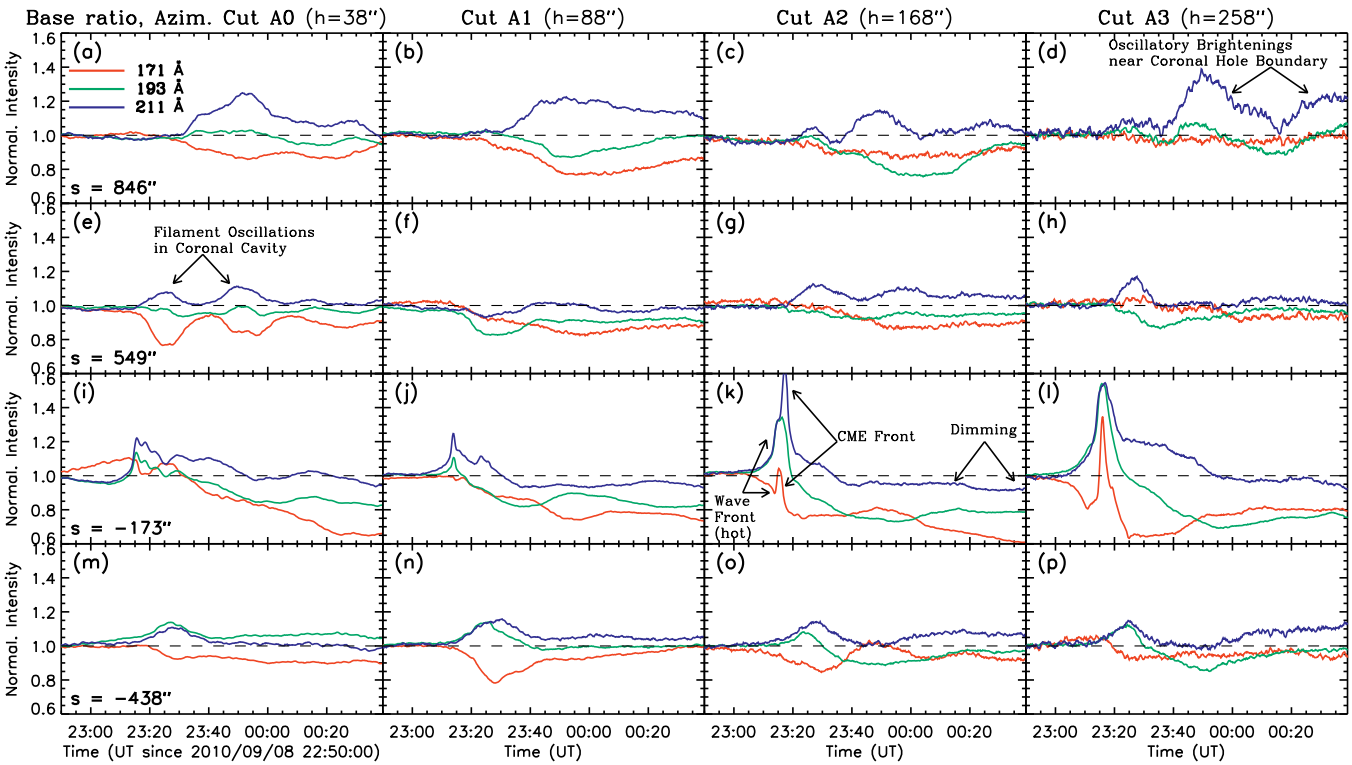

Figure 9. Base ratio temporal profiles of emission intensity from azimuthal cuts at selected positions shown in Figure 4 (plus signs there). The general trend of darkening at 171 Å and brightening at 193 and 211 Å indicates heating in the EUV wave pulse ahead of the CME.

(A color version of this figure is available in the online journal.)

2009; Chen & Wu 2011; Cheng et al. 2012) and simulations (Chen et al. 2002, 2005; Cohen et al. 2009; Downs et al. 2011, 2012) have led to a converged view about the multifaceted nature of global EUV waves. That is, a *primary (outer) fast-mode MHD wave/shock*, sometimes associated with an Hα Moreton wave (Thompson et al. 2000b; Asai et al. 2012), travels generally ahead of a *secondary (inner) slow disturbance* related to the CME-caused coronal restructuring. Along the lines of recent suggestions (e.g., Downs et al. 2011; Schrijver et al. 2011), we propose that this wave/non-wave hybrid mechanism is a general rule, rather than an exception. Under specific physical and observational circumstances, this general underlying mechanism may have different manifestations, depending on which component has the dominant observational signature. Taking the EUV wave reported by Liu et al. (2010) as an example, the low-cadence, low-sensitivity *SOHO*/EIT could miss the leading faint, diffuse wave component of 240 km s^{-1} and only capture the trailing strong, sharp non-wave fronts as slow as 80 km s^{-1}. This could cause a bias in the broad velocity distribution of 50–700 km s^{-1} obtained from EIT (Thompson & Myers 2009), the lower end of which is incompatible with fast-mode waves. Likewise, if an expanding CME drives a fast-mode wave or shock, depending on whether the stand-off distance between the wave and CME front can be spatially resolved by the instrument, one could detect both or only one component. When a separatrix surface lies in the way, the CME-caused slow component could stop, while the fast-mode component would proceed forward. As such, the single term "EIT waves" may have historically included a variety of physically distinct phenomena (Warmuth & Mann 2011).

To date, *SDO*/AIA has observed a variety of EUV waves, including those generated by mini-CMEs, emerging flux (Zheng et al. 2011, 2012), and "coronal cyclones" (Zhang & Liu 2011), as well as Kelvin–Helmholtz instability waves produced by velocity shear at CME flanks (see Ofman & Thompson 2010, 2011 for the first AIA EUV wave event reported by Liu et al. 2010; cf. Foullon et al. 2011 for a later event). These new observations, together with those presented here, add to the multitude of the EUV wave phenomenon specifically and CME/flare eruptions in general. A latest study of a large sample of $\geqslant$100 global EUV waves observed by both *SDO*/AIA and *STEREO*/EUVI has revealed an average wave velocity of 700 km s^{-1} (N. Nitta et al. 2012, in preparation). This is a strong indication that the primary EUV disturbance is a fast-mode MHD wave, a conclusion supported by many recent studies (e.g., Asai et al. 2012) and particularly the quasi-periodic wave trains ahead of the CME discovered here. The origin of their periodicity will be a subject of future investigation.

This work is supported by NASA *SDO*/AIA contract NNG04EA00C to LMSAL, W.L. and L.O. by NASA grant NNX11AO68G, and L.O. by NASA grant NNX09AG10G. We thank Cooper Downs, Spiros Patsourakos, P. F. Chen, and Keiji Hayashi for useful discussions and the referee for constructive comments that helped improve this paper. The *SOHO*/LASCO CME catalog is generated and maintained at the CDAW Data Center by NASA and The Catholic University of America in cooperation with the Naval Research Laboratory.

APPENDIX A

TECHNICAL DETAILS OF DATA ANALYSIS

As shown in Figures 3 and 7, we selected four complementing sets of narrow cuts (slits) for space–time analysis: (1) 15 radial cuts Ri ($i = 0, \ldots, 14$) of 10″ wide starting from the eruption center ($h = 49''$ above the limb at N20°.6), which serve to track the early expansion of the CME and the generation of the EUV

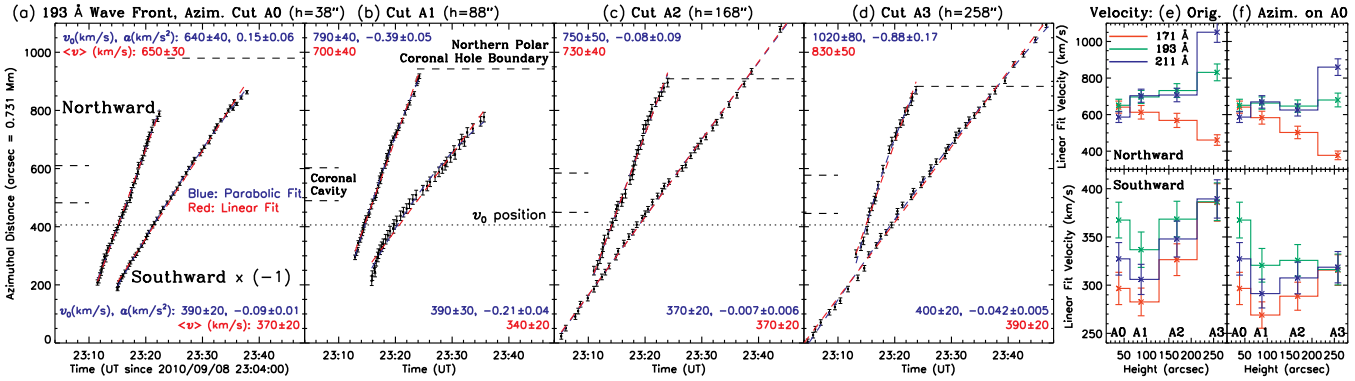

Figure 10. (a)–(d) Positions of the north- and southward 193 Å EUV wave fronts obtained from azimuthal space–time diagrams as in Figure 4. The sign of the southward distance is reversed. Overlaid dashed lines are parabolic (blue) and linear (red) fits, labeled with fitted parameters. The horizontal dotted line denotes the position where the velocity v_0 from parabolic fits is evaluated. (e) Height distribution of velocities from linear fits to wave fronts on different azimuthal cuts at 171, 193, and 211 Å. (f) Same as (e) but for velocities scaled onto the lowest cut A0, equivalent to angular velocities in the azimuthal direction with respect to the disk center. (A color version of this figure is available in the online journal.)

wave; (2) four azimuthal cuts A*i* that are 20″–30″ wide with centers located at heights of $h = 38''$, $88''$, $168''$, $258''$ and serve to track propagation at constant heights above the limb; (3) 12 vertical cuts V*i* of 20″ wide starting at the limb, which serve to provide height-dependent arrival times of propagating disturbances, with cut V6 located at the eruption center, cut V9 within the coronal cavity, and cut V11 at the coronal hole boundary; and (4) three curved cuts C*i* of 20″ wide along the funnel in which the QFP waves propagate.

Each space–time diagram was obtained by composing one-dimensional image profiles at different times along a cut. To achieve desired color scaling suitable for different features, we further applied base or running difference by subtracting an initial or immediately previous image profile, or likewise, applied base or running ratio, equivalent to differencing logarithmic profiles. We used mouse-clicks to track a moving/propagating feature whose positional uncertainties, depending on its sharpness, are typically no more than a few to ∼10″.

Bear in mind that velocities measured this way are projected velocities on the plane of sky captured within the cut. They can deviate from the true plane-of-sky velocities by a factor of $1/\cos\theta$, if the cut is at an angle θ from the direction of propagation normal to an intensity front. Significant deviations, however, only occur for large angle misalignments, say, a factor of two overestimate for $\theta = 60°$. Because this event occurs on the limb, we expect that such projection effects are rather small. The selection of complementing cuts above can also help minimize this potential bias.

STEREO A, 82° ahead of the Earth, provides complementary information at a 2.5 minute cadence of the CME–EUV wave decoupling, consistent with our and earlier results (e.g., Patsourakos et al. 2009). We thus chose to focus on new AIA observations here, but future studies using higher cadence *STEREO* data may help constrain the three-dimensional geometry of quasi-periodic wave trains.

APPENDIX B

GENERAL PROPERTIES OF GLOBAL EUV WAVE

B.1. Temperature Dependence: Heating and Cooling

The general trend of darkening at 171 Å and brightening at 193 and 211 Å at the EUV wave front, followed by a recovery in the opposite direction, as shown in Figure 4, indicates heating and subsequent cooling. Qualitatively similar behaviors were observed by *TRACE* and *STEREO*/EUVI (Wills-Davey & Thompson 1999; Dai et al. 2010) and *SDO*/AIA (Liu et al. 2010; Long et al. 2011a; Schrijver et al. 2011).

We further take horizontal slices at selected positions from Figure 4 (plus signs there) and show the resulting intensity profiles in Figure 9. The large variations near the eruption (panels (k) and (l)) are due to the erupting material and subsequent dimming, while the remaining, moderate variations result from the global EUV wave. In particular, the CME front in panel (k) appears as a sharp enhancement in all three channels, suggesting an expected density increase. Immediately ahead of it is a dip at 171 Å and a shoulder at 193 and 211 Å, indicating a heated sheath surrounding the CME front.

Within the EUV wave pulse (e.g., panel (n)), it usually takes several to 20 minutes to reach the maximum intensity variation at each wavelength, followed by a comparable or longer recovery lasting up to tens of minutes. The maximum 193 Å enhancement is about 5%–10% above the pre-event level, while the maximum 211 Å enhancement and 171 Å reduction are about two times larger on the 10%–20% level and delayed by a few minutes from the 193 Å maximum (Liu et al. 2010; Ma et al. 2011). This indicates prompt plasma heating within minutes across the characteristic temperatures of the 171, 193, and 211 Å channels, from 0.8 MK to 1.6 MK and then 2.0 MK, respectively (O'Dwyer et al. 2010; Boerner et al. 2012; cf. Kozarev et al. 2011). The subsequent recovery after the maximum toward the pre-event level is a cooling phase. Such emission variations were largely reproduced in MHD simulations and ascribed to heating by initial compression followed by cooling by restoring rarefaction in an adiabatic process associated with a compressible wave (Downs et al. 2012).

This general trend is evident in the quiet Sun to the south of the eruption. To the north, it is complicated by organized structures, such as the coronal cavity/filament and polar coronal hole boundary producing oscillatory intensity variations (panels (d) and (e)).

B.2. Kinematics and General Deceleration

To measure the velocity of the global EUV wave front, we visually identified the initial intensity change, regardless of brightening or darkening, at each distance in base-ratio space–time diagrams (e.g., Figure 4) obtained from azimuthal cuts shown in Figure 3(b). We have also tested automated methods (e.g., see Liu et al. 2010; Long et al. 2011b), but

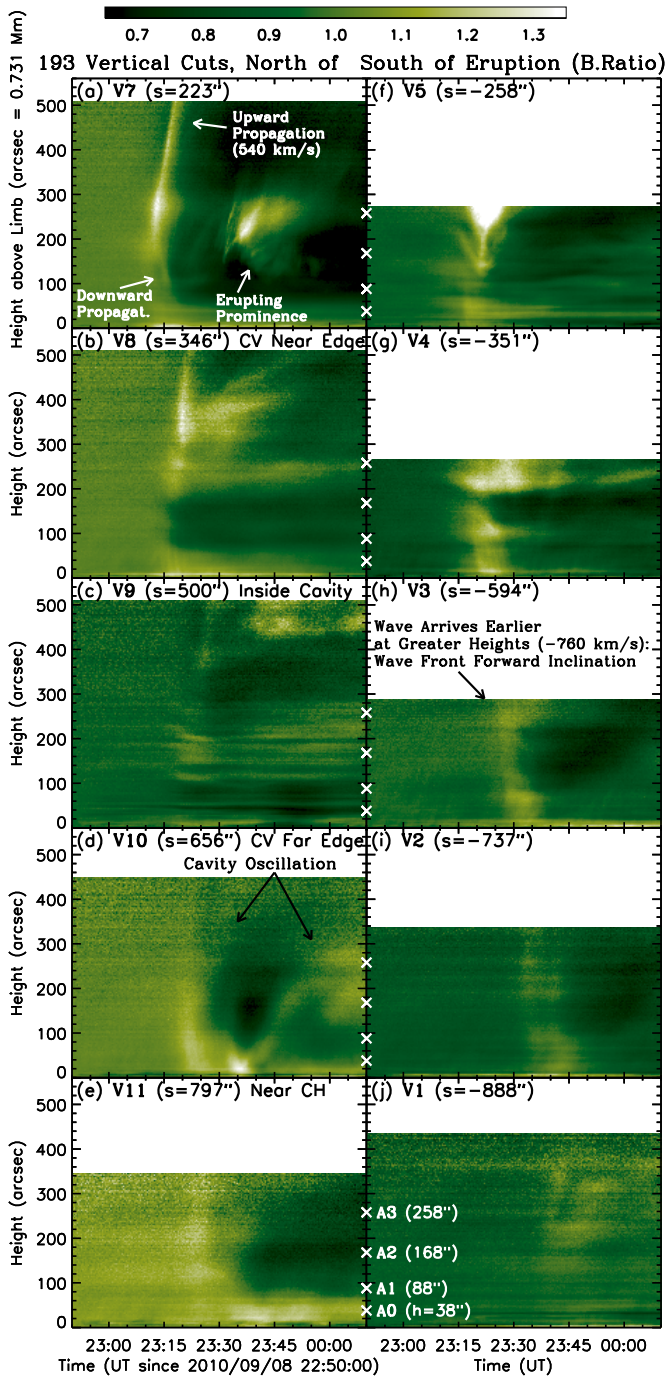

Figure 11. 193 Å base ratio space–time diagrams from selected vertical cuts in Figure 3(f), showing height-dependent arrival time of the EUV disturbance. Each panel is labeled with the azimuthal position *s* of the vertical cut, as marked by the cross signs in Figure 4(c). The cross signs here on the *y*-axis mark the heights of the azimuthal cuts A0–A3.

(A color version of this figure is available in the online journal.)

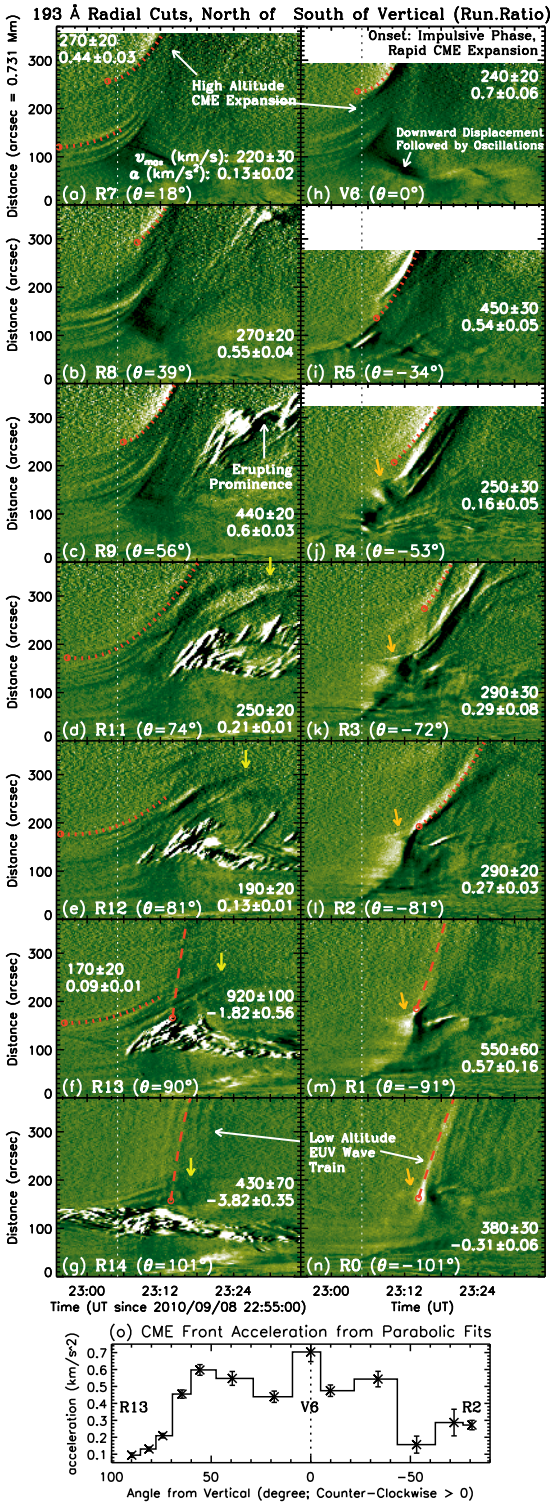

Figure 12. (a)–(n) Running-ratio space–time diagrams at 193 Å from selected radial cuts R*i* and vertical cut V6 shown in Figures 3(a) and (f). Distance is measured from the eruption center located at a height of 49″ on V6. Note the acceleration of the CME front and follow-up loops at high altitudes and the generation of the EUV wave at low altitudes. The red dotted and dashed lines are parabolic fits to the CME and EUV wave fronts, respectively, labeled with the fitted acceleration (in $\mathrm{km\,s^{-2}}$) and maximum velocity (in $\mathrm{km\,s^{-1}}$, i.e., the initial velocity for deceleration or the final velocity at $s = 370''$, top distance of the plot, for acceleration). The vertical white dotted line marks the onset of the rapid CME expansion and the flare impulsive phase at 23:05 UT. (o) The bottom panel shows the angular distribution of the CME acceleration measured from these cuts. The angle is measured from the local vertical in the counterclockwise direction.

(A color version of this figure is available in the online journal.)

all failed to consistently detect the wave front because of the complex intensity variations, as shown in Figure 9. Yet, the visual detection, with acceptable uncertainties, yielded the most consistent result.

The resulting EUV wave front positions versus time are shown in Figure 10 for the 193 Å channel, as an example, and fitted with linear (red dashed) and parabolic (blue dashed) functions. In general, both functions fit the data nearly equally

well within uncertainties, but parabolic fits yield slightly smaller χ^2 values and indicate decelerations up to $-0.88 \pm 0.17\,\mathrm{km\,s^{-2}}$ (except for the acceleration in panel (a)). At the lowest cut A0 (height $h = 38''$), linear fits give an average velocity of $650 \pm 30\,\mathrm{km\,s^{-1}}$ for the northward wave and ~50% slower at $370 \pm 20\,\mathrm{km\,s^{-1}}$ for the southward wave. This north–south asymmetry generally holds at different heights. There is a weak increase of the velocity with height, but not significant beyond uncertainties.

The EUV wave velocities measured at different wavelengths show substantial scatter (Figure 10(e) and (f)), consistent with those found by Long et al. (2008, 2011a), but their identified trend of higher velocities in cooler lines is not present here. At a given height, the velocity generally decreases from 193 to 211 and 171 Å, likely due to the delay of the same trend noted in Appendix B1.

B.3. Height Dependence and Forwardly Inclined Wave Fronts

The height dependence of the EUV wave can be examined through its arrival at vertical cuts defined in Figure 3(f). As shown in the resulting space–time diagrams of Figure 11, not far from the eruption (top three rows), a general pattern, similar across different AIA channels, is as follows. In the low corona ($h \lesssim 300'' = 220\,\mathrm{Mm}$), the initial intensity variation forms a stripe of a negative slope, indicating that the arrival of the disturbance at the vertical cut first occurs at a high altitude and then progresses toward lower altitudes; in the high corona ($h \gtrsim 300''$), the trend is opposite. For example, over a height range of 200″, the downward progression at cut V3 (south of the eruption) results in a 3 minute delay, translating to an apparent vertical velocity of $-760\,\mathrm{km\,s^{-1}}$, while the upward progression at cut V7 (north of the eruption) produces a 4.5 minute delay and an apparent velocity of $540\,\mathrm{km\,s^{-1}}$. This pattern means that the leading front of the EUV wave near the eruption has a sphere-like shape (Veronig et al. 2010; Selwa et al. 2012): viewed from the eruption center, the front is upwardly concave in the high corona and *forwardly inclined* toward the solar surface in the low corona, as further discussed in Section 6.

The delayed arrival at the vertical cut V8 shown in Figure 5(k), for example, can be used to reconstruct the corresponding wave front. For each height h, we first interpolated the azimuthal wave velocity $v(h)$ from those average velocities measured on cuts A0–A3 at different heights (see Figure 10). We then obtained the azimuthal distance traveled from the actual arrival time $t(h)$ to a reference arrival time of $t(0) = 23{:}16{:}55$ UT at the coronal base ($h = 0$), $\Delta s(h) = [t(0) - t(h)]v(h)$. This distance was added to the azimuthal position $s_{\mathrm{cut}}(h)$ of this vertical cut measured from the eruption center to obtain the position of the instantaneous wave front at $t(0)$, $s(h) = s_{\mathrm{cut}}(h) + \Delta s(h)$. Repeating this for all heights and then transforming the azimuthal positions back to the Cartesian coordinates gave the resulting wave front, as shown in red in Figure 5(l).

APPENDIX C

CME KINEMATICS AND EARLY EXPANSION

Figure 12 shows the expansion in different directions of coronal loops involved in the CME, as captured in radial cuts defined in Figure 3(a). Strong acceleration ($a > 0.4\,\mathrm{km\,s^{-2}}$) only occurs within an angular range $-50^\circ \leqslant \theta \leqslant 70^\circ$ of the local vertical at the eruption center (panel (o)). In this range, the CME experiences a two-phase, slow to fast expansion (Sterling & Moore 2005), the transition of which occurs at 23:05 UT, the beginning of the flare impulsive phase. The early phase has an acceleration $\lesssim 0.1\,\mathrm{km\,s^{-2}}$ and maximum velocity $\sim 100\,\mathrm{km\,s^{-1}}$ (panel (a)). The largest acceleration of $0.70 \pm 0.06\,\mathrm{km\,s^{-2}}$ in the late-phase takes place in the vertical direction (panel (h)), reaching $240 \pm 20\,\mathrm{km\,s^{-1}}$ at the edge of the AIA FOV. Comparable acceleration possibly continues into the *SOHO*/LASCO FOV (1.5–30 $R_\odot$), as shown by the dotted line in the inset of Figure 2(c). The CME then decelerates at $a = -0.019 \pm 0.005\,\mathrm{km\,s^{-2}}$ with initial and average velocities of $v_{\mathrm{max}} = 990 \pm 70\,\mathrm{km\,s^{-1}}$ and $\langle v \rangle = 820 \pm 40\,\mathrm{km\,s^{-1}}$, according to the CME catalog (https://cdaw.gsfc.nasa.gov/CME_list).

Beyond the angular range of $-50^\circ \leqslant \theta \leqslant 70^\circ$, the CME acceleration remains below $0.3\,\mathrm{km\,s^{-2}}$, with no two-phase distinction but a north-south asymmetry. To the north of the vertical, the expanding loops gradually slow down and/or fade away (panel (e)). This first occurs at the lowest cut and progresses toward cuts at greater heights, as indicated by the short yellow arrows. To the south, the early slow expansion is absent, but a sudden brightening caused by a rapid *downward* expansion of some loops (see movie 1C), indicated by the short orange arrows, takes place sequentially from cut R4 to R0. It is at the outermost edge of this brightening near the coronal base, $s_0 = 150'' = 110\,\mathrm{Mm}$ from the eruption center, that the southward global EUV wave is launched at 23:14:20 UT (panels (m) and (n)). Its northward counterpart is first detected at a similar distance 3 minutes earlier.

We note in panel (h) that, in the vertical direction, some loops at the eruption center are pushed downward from an initial height of $h_0 = 150''$ (with the 49″ height of the origin of the cut included), followed by transverse oscillations. In lateral directions, at the onset of the rapid CME expansion (vertical dotted line), all participating loops are also located approximately beyond a distance $s_0 = 110\,\mathrm{Mm}$ from the eruption center. This indicates that the rapid expansion involves the entire active region of $r_{\mathrm{AR}} = 110\,\mathrm{Mm}$ in radius and originates at its center of height $h_0 = 110\,\mathrm{Mm}$. These observations imply that this expansion, with a significant downward component, may play a key role in driving the EUV wave (see more discussion in Section 6.2).

APPENDIX D

ESTIMATES OF EUV WAVE ENERGY AND CAVITY MAGNETIC FIELD

We can utilize the oscillations of the coronal cavity to estimate the energy budget of the global EUV wave (see, e.g., Ballai et al. 2005) and the cavity magnetic field strength, i.e., by coronal seismology. These are order-of-magnitude estimates with comparable uncertainties.

The cavity has a diameter $D_{\mathrm{cav}} = 135'' = 99\,\mathrm{Mm}$ measured on azimuthal cut A2 in Figure 5(c). Its embedded filament, likely underneath the axis of the flux rope running along its full length (e.g., Low & Hundhausen 1995), has been quite stable for a week before this event. It was best seen a few days earlier (say, September 4, at http://www.solarmonitor.org), located at N50° on the disk, spanning a longitude range of 35° and a length of $L_{\mathrm{cav}} = 273\,\mathrm{Mm}$. Assuming that cavity is a cylinder of such a dimension, its volume is $V_{\mathrm{cav}} = \pi(D_{\mathrm{cav}}/2)^2 L_{\mathrm{cav}}$. We adopt an average electron density of $n_e = 1 \times 10^9\,\mathrm{cm^{-3}}$ of the tenuous cavity and its dense filament combined (Vásquez et al. 2009) and thus $\rho = n_e m_p = 1.7 \times 10^{-15}\,\mathrm{g\,cm^{-3}}$. Its total mass is $m_{\mathrm{cav}} = \rho V_{\mathrm{cav}} = 3.5 \times 10^{15}\,\mathrm{g}$, comparable to a typical CME mass (Aschwanden et al. 2009). Now, taking a

velocity amplitude of $v_{osc} = 9\,km\,s^{-1}$, we obtain the kinetic energy of the cavity of $E_{k,cav} = m_{cav}v_{osc}^2/2 \sim 2 \times 10^{27}$ erg and energy per unit length along its axis of $e_{k,cav} = E_{k,cav}/L_{cav}$. We further assume that such an energy is uniformly distributed in space at the same projected distance from the eruption center, $s = 450'' = 329\,Mm$, measured on cut A2 (Figure 5(c)), as a consequence of a surface-like wave in the low corona. Then, the global EUV wave energy is $E_{wv} = e_{k,cav}(2\pi s) \sim 1 \times 10^{28}$ erg. Both energies are 3–4 orders of magnitude smaller than the kinetic energy $E_{k,CME} \sim 1 \times 10^{31}$ erg of the CME, assumed at the same mass as the cavity moving at $820\,km\,s^{-1}$ measured by *SOHO*/LASCO. This wave energy is, however, 100 times greater than that of another EUV wave and of a typical nanoflare (Ballai et al. 2005).

These transverse oscillations are likely fast kink modes. In this case, the period for the Nth harmonics is $P = 2l/(Nc_k)$, where l is the loop length and $c_k \sim v_A \sim v_f$ is the kink speed in low-β plasma with a loop density of the same order of the surrounding plasma (v_A and v_f being the Alfvén and fast-mode speeds, respectively). Using the measured average period of 27.6 minutes for the fundamental mode $N = 1$ and assuming $c_k = 980\,km\,s^{-1}$, we have $l = Pc_k/2 \approx 800\,Mm \approx 3L_{cav}$, where $L_{cav} = 273\,Mm$ is the cavity's axial length measured above. This gives a pitch angle of $\theta = \arccos(L_{cav}/l) = \arccos(1/3) \sim 70^\circ$, implying an expected, highly twisted flux rope (Carter & Erdélyi 2008). If we adopt a typical density of $n_e = 2 \times 10^8\,cm^{-3}$ ($\rho = n_e m_p = 3 \times 10^{-16}\,g\,cm^{-3}$; from Schmit & Gibson 2011) for the coronal cavity, we obtain a magnetic field strength of $B = v_A\sqrt{4\pi\rho} \sim 6\,G$.

REFERENCES

Afanasyev, A. N., & Uralov, A. M. 2011, Sol. Phys., 273, 479
Asai, A., Ishii, T. T., Isobe, H., et al. 2012, ApJ, 745, L18
Aschwanden, M. J. 2004, Physics of the Solar Corona: An Introduction (Berlin: Springer)
Aschwanden, M. J., Nitta, N. V., Wuelser, J.-P., et al. 2009, ApJ, 706, 376
Aschwanden, M. J., & Schrijver, C. J. 2011, ApJ, 736, 102
Attrill, G. D. R., Harra, L. K., van Driel-Gesztelyi, L., & Démoulin, P. 2007, ApJ, 656, L101
Bain, H. M., Krucker, S., Glesener, L., & Lin, R. P. 2012, ApJ, 750, 44
Balasubramaniam, K. S., Cliver, E. W., Pevtsov, A., et al. 2010, ApJ, 723, 587
Ballai, I. 2007, Sol. Phys., 246, 177
Ballai, I., Erdélyi, R., & Pintér, B. 2005, ApJ, 633, L145
Berger, T., Testa, P., Hillier, A., et al. 2011, Nature, 472, 197
Boerner, P. F., Edwards, C. G., Lemen, J. R., et al. 2012, Sol. Phys., 275, 41
Carter, B. K., & Erdélyi, R. 2008, A&A, 481, 239
Chen, F., Ding, M. D., Chen, P. F., & Harra, L. K. 2011, ApJ, 740, 116
Chen, P. F. 2006, ApJ, 641, L153
Chen, P. F. 2011, Living Rev. Sol. Phys., 8, 1
Chen, P. F., Fang, C., & Shibata, K. 2005, ApJ, 622, 1202
Chen, P. F., Wu, S. T., Shibata, K., & Fang, C. 2002, ApJ, 572, L99
Chen, P. F., & Wu, Y. 2011, ApJ, 732, L20
Cheng, X., Zhang, J., Olmedo, O., et al. 2012, ApJ, 745, L5
Cohen, O., Attrill, G. D. R., Manchester, W. B., & Wills-Davey, M. J. 2009, ApJ, 705, 587
Dai, Y., Auchère, F., Vial, J., Tang, Y. H., & Zong, W. G. 2010, ApJ, 708, 913
Delannée, C. 2000, ApJ, 545, 512
Delannée, C., Hochedez, J.-F., & Aulanier, G. 2007, A&A, 465, 603
Delannée, C., Török, T., Aulanier, G., & Hochedez, J. 2008, Sol. Phys., 247, 123
Downs, C., Roussev, I. I., van der Holst, B., Lugaz, N., & Sokolov, I. V. 2012, ApJ, 750, 134
Downs, C., Roussev, I. I., van der Holst, B., et al. 2011, ApJ, 728, 2
Fisher, G. H., Bercik, D. J., Welsch, B. T., & Hudson, H. S. 2012, Sol. Phys., 277, 59
Foullon, C., Verwichte, E., Nakariakov, V. M., Nykyri, K., & Farrugia, C. J. 2011, ApJ, 729, L8
Gallagher, P. T., & Long, D. M. 2011, Space Sci. Rev., 158, 365
Gibson, S. E., Kucera, T. A., Rastawicki, D., et al. 2010, ApJ, 724, 1133
Gilbert, H. R., & Holzer, T. E. 2004, ApJ, 610, 572
Gopalswamy, N., Yashiro, S., Temmer, M., et al. 2009, ApJ, 691, L123
Grechnev, V. V., Afanasyev, A. N., Uralov, A. M., et al. 2011a, Sol. Phys., 273, 461
Grechnev, V. V., Uralov, A. M., Chertok, I. M., et al. 2011b, Sol. Phys., 273, 433
Harra, L. K., & Sterling, A. C. 2003, ApJ, 587, 429
Harra, L. K., Sterling, A. C., Gömöry, P., & Veronig, A. 2011, ApJ, 737, L4
Hershaw, J., Foullon, C., Nakariakov, V. M., & Verwichte, E. 2011, A&A, 531, A53
Hudson, H. S., Fletcher, L., Fisher, G. H., Abbett, W. P., & Russell, A. 2012, Sol. Phys., 277, 77
Khan, J. I., & Aurass, H. 2002, A&A, 383, 1018
Kienreich, I. W., Muhr, N., Veronig, A., et al. 2012, Sol. Phys., in press (arXiv:1204.6472)
Kienreich, I. W., Temmer, M., & Veronig, A. M. 2009, ApJ, 703, L118
Kosovichev, A. G., & Zharkova, V. V. 1999, Sol. Phys., 190, 459
Kozarev, K. A., Korreck, K. E., Lobzin, V. V., Weber, M. A., & Schwadron, N. A. 2011, ApJ, 733, L25
Lemen, J. R., Title, A. M., Akin, D. J., et al. 2012, Sol. Phys., 275, 17
Li, T., Zhang, J., Yang, S.-H., & Liu, W. 2012a, Res. Astron. Astrophys., 12, 104
Li, T., Zhang, J., Yang, S.-H., & Liu, W. 2012b, ApJ, 746, 13
Liu, W., Berger, T. E., Title, A. M., & Tarbell, T. D. 2009a, ApJ, 707, L37
Liu, W., Berger, T. E., Title, A. M., Tarbell, T. D., & Low, B. C. 2011a, ApJ, 728, 103
Liu, W., Liu, S., Jiang, Y. W., & Petrosian, V. 2006, ApJ, 649, 1124
Liu, W., Nitta, N. V., Schrijver, C. J., Title, A. M., & Tarbell, T. D. 2010, ApJ, 723, L53
Liu, W., Title, A. M., Zhao, J., et al. 2011b, ApJ, 736, L13
Liu, W., Wang, T.-J., Dennis, B. R., & Holman, G. D. 2009b, ApJ, 698, 632
Long, D. M., DeLuca, E. E., & Gallagher, P. T. 2011a, ApJ, 741, L21
Long, D. M., Gallagher, P. T., McAteer, R. T. J., & Bloomfield, D. S. 2008, ApJ, 680, L81
Long, D. M., Gallagher, P. T., McAteer, R. T. J., & Bloomfield, D. S. 2011b, A&A, 531, A42
Low, B. C., & Hundhausen, J. R. 1995, ApJ, 443, 818
Ma, S., Raymond, J. C., Golub, L., et al. 2011, ApJ, 738, 160
Ma, S., Wills-Davey, M. J., Lin, J., et al. 2009, ApJ, 707, 503
Mann, G. 1995, J. Plasma Phys., 53, 109
Moreton, G. E. 1960, AJ, 65, 494
Moses, D., Clette, F., Delaboudinière, J., et al. 1997, Sol. Phys., 175, 571
Muhr, N., Veronig, A. M., Kienreich, I. W., Temmer, M., & Vršnak, B. 2011, ApJ, 739, 89
Muhr, N., Vršnak, B., Temmer, M., Veronig, A. M., & Magdalenić, J. 2010, ApJ, 708, 1639
Nakariakov, V. M., & Melnikov, V. F. 2009, Space Sci. Rev., 149, 119
Nakariakov, V. M., & Verwichte, E. 2005, Living Rev. Sol. Phys., 2, 3
Narukage, N., Hudson, H. S., Morimoto, T., et al. 2002, ApJ, 572, L109
Neupert, W. M. 1968, ApJ, 153, L59
Ning, Z., & Cao, W. 2010, ApJ, 717, 1232
O'Dwyer, B., Del Zanna, G., Mason, H. E., Weber, M. A., & Tripathi, D. 2010, A&A, 521, A21
Ofman, L. 2009, Space Sci. Rev., 149, 153
Ofman, L., & Aschwanden, M. J. 2002, ApJ, 576, L153
Ofman, L., Liu, W., Title, A., & Aschwanden, M. 2011, ApJ, 740, L33
Ofman, L., & Sui, L. 2006, ApJ, 644, L149
Ofman, L., & Thompson, B. J. 2002, ApJ, 574, 440
Ofman, L., & Thompson, B. J. 2010, American Geophysical Union, Fall Meeting 2010, abstract #SH14A-02
Ofman, L., & Thompson, B. J. 2011, ApJ, 734, L11
Okamoto, T. J., Nakai, H., Keiyama, A., et al. 2004, ApJ, 608, 11244
Olmedo, O., Vourlidas, A., Zhang, J., & Cheng, X. 2012, ApJ, submitted
Patsourakos, S., & Vourlidas, A. 2009, ApJ, 700, L182
Patsourakos, S., & Vourlidas, A. 2012, arXiv:1203.1135
Patsourakos, S., Vourlidas, A., & Kliem, B. 2010a, A&A, 522, A100
Patsourakos, S., Vourlidas, A., & Stenborg, G. 2010b, ApJ, 724, L188
Patsourakos, S., Vourlidas, A., Wang, Y. M., Stenborg, G., & Thernisien, A. 2009, Sol. Phys., 259, 49
Pesnell, W. D., Thompson, B. J., & Chamberlin, P. C. 2012, Sol. Phys., 275, 3
Pomoell, J., Vainio, R., & Kissmann, R. 2008, Sol. Phys., 253, 249
Roberts, B., Edwin, P. M., & Benz, A. O. 1984, ApJ, 279, 857
Schmidt, J. M., & Ofman, L. 2010, ApJ, 713, 1008
Schmit, D. J., & Gibson, S. E. 2011, ApJ, 733, 1
Schrijver, C. J., Aulanier, G., Title, A. M., Pariat, E., & Delannée, C. 2011, ApJ, 738, 167

Schrijver, C. J., Elmore, C., Kliem, B., Török, T., & Title, A. M. 2008, ApJ, 674, 586
Selwa, M., Poedts, S., & DeVore, C. R. 2012, ApJ, 747, L21
Shen, Y. D., & Liu, Y. 2012, ApJ, 753, 53
Sterling, A. C., & Moore, R. L. 2005, ApJ, 630, 1148
Sun, X., Hoeksema, J. T., Liu, Y., et al. 2012, ApJ, 748, 77
Sych, R., Nakariakov, V. M., Karlicky, M., & Anfinogentov, S. 2009, A&A, 505, 791
Temmer, M., Veronig, A. M., Gopalswamy, N., & Yashiro, S. 2011, Sol. Phys., 273, 421
Temmer, M., Veronig, A. M., Vršnak, B., et al. 2008, ApJ, 673, L95
Temmer, M., Vršnak, B., Žic, T., & Veronig, A. M. 2009, ApJ, 702, 1343
Thompson, B. J., Cliver, E. W., Nitta, N., Delannée, C., & Delaboudinière, J. 2000a, Geophys. Res. Lett., 27, 1431
Thompson, B. J., Gurman, J. B., Neupert, W. M., et al. 1999, ApJ, 517, L151
Thompson, B. J., & Myers, D. C. 2009, ApJS, 183, 225
Thompson, B. J., Plunkett, S. P., Gurman, J. B., et al. 1998, Geophys. Res. Lett., 25, 2465
Thompson, B. J., Reynolds, B., Aurass, H., et al. 2000b, Sol. Phys., 193, 161
Thompson, W. T., Kliem, B., & Török, T. 2012, Sol. Phys., 276, 241
Tripathi, D., Isobe, H., & Jain, R. 2009, Space Sci. Rev., 149, 283
Uchida, Y. 1968, Sol. Phys., 4, 30
Uchida, Y. 1970, PASJ, 22, 341
Vásquez, A. M., Frazin, R. A., & Kamalabadi, F. 2009, Sol. Phys., 256, 73
Veronig, A. M., Brown, J. C., Dennis, B. R., et al. 2005, ApJ, 621, 482
Veronig, A. M., Gomory, P., Kienreich, I. W., et al. 2011, ApJ, 743, L10
Veronig, A. M., Muhr, N., Kienreich, I. W., Temmer, M., & Vršnak, B. 2010, ApJ, 716, L57
Veronig, A. M., Temmer, M., & Vršnak, B. 2008, ApJ, 681, L113
Vršnak, B., & Cliver, E. W. 2008, Sol. Phys., 253, 215
Vršnak, B., & Lulić, S. 2000, Sol. Phys., 196, 157
Vršnak, B., Ruzdjak, V., Zlobec, P., & Aurass, H. 1995, Sol. Phys., 158, 331
Vršnak, B., Warmuth, A., Brajša, R., & Hanslmeier, A. 2002, A&A, 394, 299
Wang, H., & Liu, C. 2010, ApJ, 716, L195
Wang, T., Ofman, L., Davila, J. M., & Su, Y. 2012, ApJ, 751, L27
Wang, Y. 2000, ApJ, 543, L89
Warmuth, A. 2007, in Lecture Notes in Physics, Vol. 725, The High Energy Solar Corona: Waves, Eruptions, Particles, ed. K.-L. Klein & A. L. MacKinnon (Berlin: Springer), 107
Warmuth, A. 2011, Plasma Phys. Control. Fusion, 53, 124023
Warmuth, A., & Mann, G. 2011, A&A, 532, A151
Warmuth, A., Vršnak, B., Aurass, H., & Hanslmeier, A. 2001, ApJ, 560, L105
Warmuth, A., Vršnak, B., Magdalenić, J., Hanslmeier, A., & Otruba, W. 2004, A&A, 418, 1101
White, R. S., & Verwichte, E. 2012, A&A, 537, A49
White, S. M., Balasubramanian, K. S., & Cliver, E. W. 2011, in SPD Meeting 42, 13.07, Bulletin of the American Astronomical Society, Vol. 43, 2011
White, S. M., & Thompson, B. J. 2005, ApJ, 620, L63
Wills-Davey, M. J., & Attrill, G. D. R. 2009, Space Sci. Rev., 149, 325
Wills-Davey, M. J., DeForest, C. E., & Stenflo, J. O. 2007, ApJ, 664, 556
Wills-Davey, M. J., & Thompson, B. J. 1999, Sol. Phys., 190, 467
Wu, S. T., Zheng, H., Wang, S., et al. 2001, J. Geophys. Res., 106, 25089
Wuelser, J.-P., Lemen, J. R., Tarbell, T. D., et al. 2004, Proc. SPIE, 5171, 111
Zhang, J., Dere, K. P., Howard, R. A., Kundu, M. R., & White, S. M. 2001, ApJ, 559, 452
Zhang, J., & Liu, Y. 2011, ApJ, 741, L7
Zhao, X. H., Wu, S. T., Wang, A. H., et al. 2011, ApJ, 742, 131
Zharkov, S., Green, L. M., Matthews, S. A., & Zharkova, V. V. 2011, ApJ, 741, L35
Zheng, R., Jiang, Y., Hong, J., et al. 2011, ApJ, 739, L39
Zheng, R., Jiang, Y., Yang, J., et al. 2012, ApJ, 747, 67
Zhukov, A. N. 2011, J. Atmos. Sol.–Terr. Phys., 73, 1096
Zhukov, A. N., & Auchère, F. 2004, A&A, 427, 705
Zhukov, A. N., Rodriguez, L., & de Patoul, J. 2009, Sol. Phys., 259, 73
Žic, T., Vršnak, B., Temmer, M., & Jacobs, C. 2008, Sol. Phys., 253, 237